Published in final edited form as:

Neurochem Res. 2023 April ; 48(4): 1191–1210. doi:10.1007/s11064-022-03663-4.

Chronic stress impairs the structure and function of astrocyte networks in an animal model of depression

Sydney Aten[1,¶], **Yixing Du**[1], **Olivia Taylor**[1], **Courtney Dye**[1], **Kelsey Collins**[1], **Matthew Thomas**[1], **Conrad Kiyoshi**[1,#], **Min Zhou**[1,*]

[1]Department of Neuroscience, Ohio State University Wexner Medical Center, Columbus, OH 43210, USA

Abstract

Astrocytes are key contributors to the pathophysiology of major depression. Evidence in rodents shows that chronic stress is associated with a decrease in the number of GFAP-immunoreactive astrocytes within the cortex in addition to changes in the complexity and length of astrocyte processes. Furthermore, postmortem brains of individuals with depression have revealed a decrease in astrocyte density. Notably, astrocytes are extensively coupled to one another through gap junctions to form a network, or syncytium, and we have previously demonstrated that syncytial isopotentiality is a mechanism by which strong electrical coupling allows astrocytes to function as an efficient system with respect to brain homeostasis. Interestingly, the question of how astrocyte network function changes following chronic stress is yet to be elucidated. Here, we sought to examine the effects of chronic stress on *network-level* astrocyte (dys)function. Using a transgenic astrocyte reporter mouse, a six-week unpredictable chronic mild stress (UCMS) paradigm as a rodent model of major depression, and immunohistochemical approaches, we show that the morphology of individual astrocytes is altered by chronic stress exposure. Additionally, using novel electrophysiological techniques, we found that UCMS impairs the syncytial coupling strength of astrocytes within the hippocampus and prefrontal cortex - two brain regions that have been implicated in the regulation of mood. Together, these findings reveal that chronic stress leads to alterations in gap junction coupling, raising the prospect that both individual *and* network-level astrocyte functionality are important in the etiology of major depression and other neuropsychiatric disorders.

[*]Corresponding Author**:** Dr. Min Zhou, Department of Neuroscience, Ohio State University, Graves Hall, Rm 4066C, 333 W. 10th Ave. Columbus, OH 43210, Phone: (614) 366-9406, Fax: (614) 688-8742, zhou.787@osu.edu.

[¶]:Present address: Department of Neurology, Division of Sleep Medicine, and Program in Neuroscience, Harvard Medical School, Beth Israel Deaconess Medical Center, Boston, MA.

[#]:Present address: Northern Marianas College, Saipan, MP.

Author Contributions

All authors contributed to the study conception and design. Conceptualization, data acquisition, data analysis/interpretation, drafting of original manuscript, and manuscript revisions were performed by Sydney Aten. Conceptualization, data acquisition, data analysis/interpretation, and manuscript revisions were performed by Yixing Du. Olivia Taylor, Courtney Dye, and Kelsey Collins performed data analysis and assisted in manuscript revision. Matthew Thomas assisted with data acquisition and manuscript revision. Conrad Kiyoshi assisted with project conceptualization and manuscript revision. Min Zhou participated in project conceptualization, data interpretation and manuscript revision. All authors read and approved the final manuscript.

Competing Interests

The authors declare no competing financial or non-financial interests.

Ethics Approval

Animal care protocols and methods were approved by the Ohio State University's Institutional Animal Care and Use Committee (IACUC).

Keywords

Unpredictable Chronic Mild Stress (UCMS); Prefrontal Cortex; Hippocampus; Astrocyte Syncytial Isopotentiality; CUBIC Tissue Clearing; Patch Clamp

Introduction

The lifetime incidence of Major Depressive Disorder (MDD) in adults is over 20% [1]. Indeed, depression is one of the leading causes of disability around the world with over 4% of the global population (or over 320 million people) afflicted by the disorder [2]. Notably, chronic exposure to stressful situations or life events is thought to be a major player in the development of major depression [3, 4]. From a basic research perspective, while much literature over the years has elucidated the synaptic dysfunctions/neuronal perturbations that are often associated with chronic stress and depressive-like behaviors [5–7], there is still much to be learned about the role of astrocytes in depressed states.

Astrocytes are connected via gap junctions to form an extensive network within the CNS. Gap junctional coupling mediates intercellular communication by providing continuity between the cytoplasm of adjacent cells [8–10]. Hence, gap junctions are critical components in the establishment of a functional astrocyte syncytium whereby these intercellular channels allow astrocytes to be electrically coupled such that they are in a state of ‘syncytial isopotentiality’ - a phenomenon recently discovered by our lab [11, 12]. Electrical coupling allows astrocytes to function as a single, cohesive unit, and gap junction coupling endows astrocytes the ability to spatially redistribute small ions, nutrients, and other metabolites - molecules important for the regulation of neuronal activity, cell signaling, and energy metabolism [13–21]. Given the importance of gap junctions in brain homeostasis, it is reasonable to postulate that altered gap junction coupling may lead to the manifestation of many behaviors that are often observed in individuals with neurological disease/disorders -such as major depression.

Accumulating evidence has suggested that astrocyte (dys)function may be key in the development of anhedonic behaviors observed in animal models of depression. Along these lines, a reduction in astrocyte process length and/or volume has been observed after chronic stress paradigms [22–24]. Further, using sequencing-based approaches, several recent studies have shown that acute and chronic stress leads to alterations in gene expression associated with astrocyte plasticity, in addition to alterations in the expression of connexin subunits - proteins that comprise gap junctions [20, 25]. These studies reveal essential information about the morphological and transcriptomic changes that occur within astrocytes and accompany chronic stress. However, whether astrocyte *network* anatomy and function are altered in response to chronic stress is not yet known.

Here, we utilized an *Aldh1l1*-eGFP astrocyte reporter mouse line and a six-week unpredictable chronic mild stress (UCMS) model of depression to examine how both individual and network-level astrocyte anatomy and function change in response to stress. Using immunofluorescence and tissue clearing methodologies, we found that astrocytes in the hippocampus and/or PFC display a reduction in process length/area. Further, we used the

syncytial isopotentiality measurement recently developed by our lab to detect stress-induced changes in the coupling strength of the astrocyte syncytial network [12]. While there are several methods for analyzing gap junctional coupling, the electrical coupling measurement is based on the open probability of gap junction channels. Therefore, it has the highest sensitivity for detecting subtle changes in the strength of syncytial coupling [26]. Using this method, we demonstrate that chronic stress leads to a decrease in astrocyte syncytial coupling strength. These findings suggest that alterations in gap junction coupling between astrocytes may contribute (at least in part) to the behavioral manifestations that are often observed in individuals with MDD.

Materials and Methods

Mice

All experiments were performed in BAC *Aldh1l1*-eGFP transgenic adult (i.e., ~6-12 weeks of age) animals. These mice have previously been described [27–29]. All mice were housed in a 12:12 LD cycle and were given ad libitum access to water and food. Of note, only male animals were used for the immunohistochemical/tissue clearing experiments. However, due to the limited number of transgenic animals available, both male and female mice were used for the remaining electrophysiological experiments. Because no significant sex difference was observed in these electrophysiology studies, data from both sexes was combined for data analysis.

Unpredictable Chronic Mild Stress (UCMS) paradigm

The unpredictable chronic mild stress (UMCS) paradigm has been used to model depression observed in human subjects, and our specific model is adapted from previously published papers [30–33]. In brief, animals were exposed to 2-3 unpredictable mild stressors per day for a period of six weeks. The stressors were performed at random times throughout the day to avoid habituation. Every animal within the ‘stress’ group was exposed to the same stressors. Anxiety and depression-related behaviors were then profiled using the open field test, tail suspension test, and sucrose splash test. Body weight and coat state was also monitored each week.

Coat state scoring

The fur/coat state of each mouse was monitored weekly by an individual blind to stress condition. This scoring system was adapted from previously described coat rating scales/protocols [34–36]. In brief, the coat for each mouse was assigned a score ranging from 1 to 4, and this score was determined by assigning individual scores to 8 total body regions: head, neck, dorsal coat, ventral coat, tail, forelimbs, hindlimbs, and genital region. The final score was then calculated as the sum of the score for each body part divided by 8 (the number of body regions). The scoring system for fur state is noted below for reference:

1. coat is extremely shiny and smooth; no bald patches or discoloration
2. coat is largely smooth, but a few ‘spikey’ patches can be noted
3. small ‘bald’ patches are noticeable and slight discoloration is also apparent

4. several bald patches can be noted; fur is not shiny and discoloration and/or many ‘spikey’ fur patches are obvious

Open field test

The open field test was used to examine general locomotor activity and anxiety [37] and was conducted under dim white light approximately 3 hours after ‘lights on’ (Zeitgeber Time 3, ZT3). In brief, animals were placed in the arena and were given 10 minutes to explore. A video camera was placed above the arena and was used to record each trial. The bottom surface and the walls of the arena were wiped with ethanol between trials. The number of center entries and the total time spent in the center of the arena were analyzed by an experimenter blind to stress condition.

Tail suspension test

The tail suspension test was used to assay the animal stress [38]. Briefly, mice were hung upside down for a 6-minute period, and a video camera recorded each trial. The total time spent immobile (i.e., the time spent freezing) and the latency to the first immobile episode were analyzed by an experimenter blind to stress condition. The tail suspension test was performed after the open field test, and it was conducted under dim white light at approximately ZT3-5.

Sucrose splash test

The sucrose splash test was adapted as a readout of self-care [39]. Briefly, while in the home cage, the dorsal coat of each mouse was sprayed with three ‘squirts’ of a 10% sucrose solution, which dirties the fur and causes the animals to initiate grooming behavior. A video camera then recorded the grooming behavior (which was defined as the mouse licking their dorsal coat to clean off the sucrose). The number of grooming bouts and the total time spent grooming during the 5-minute period were subsequently analyzed. Animals (control and stressed) that showed no licking bouts within the 5-minute period were not included in analysis. Of note, this test was conducted at ~ZT5.

Tissue processing for immunofluorescence

Tissue was processed using methods adapted from previously published papers [37, 40, 41]. Along these lines, mice were sacrificed via rapid cervical dislocation, brains were placed into artificial cerebral spinal fluid (aCSF) and the tissue blocks containing the hippocampus and prefrontal cortex (PFC) were then cut into ~600 μm thick sections on a MicroSlicer™ Zero IN Vibratome (Ted Pella, Redding, CA). Sections were then fixed in 4% paraformaldehyde (PFA) - which was diluted in 1X phosphate-buffered saline (PBS) - for 6 hours at 4C. These 600 μm thick sections were then cryoprotected overnight in 30% sucrose solution (in 1X PBS). Finally, 30 μm thick sections were cut using a freezing microtome.

Immunofluorescent staining, imaging, and image analysis

Labeling of tissue for immunofluorescence experiments was adapted from a protocol published in a recent study [42]. For visualization of the *Aldh1l1*-eGFP transgene expression throughout the brain (serial sections), 30 μm thick tissue sections were mounted onto a

slide (i.e., no primary antibody was applied), and 10X images were acquired using a Leica SP8 confocal microscope. Individual 10X images were then stitched/merged using LASX software.

To visualize *Aldh1l1*-eGFP expression with the astrocytic marker GFAP and the neuronal marker NeuN, brain sections were washed/permeabilized in PBS triton (PBST), blocked in 3% bovine serum alum (BSA)/PBST for 1 hour at room temperature before overnight incubation in the following primary antibodies (diluted in PBST): chicken anti-GFP (1:40,000; Aves Cat # GFP-1010) to enhance the eGFP transgene, rat anti-GFAP (1: 20,000 Invitrogen, Cat # 13-0300), and guinea pig anti-NeuN (1:5,000 Millipore Sigma, Cat # ABN90). The next day (after washes), sections were incubated for 2 hours in Alexa Fluor 488 goat anti-chicken IgY, Alexa Fluor 594 goat anti-rat IgY, and anti-guinea pig Cy5 respectively (1:1500 each diluted in PBST). Tissue was then incubated in Hoechst (1:3000 diluted in PBST) for 10 min before being washed, mounted, and coverslipped with Fluoromount G. 20X images were then acquired on a Leica SP8 confocal to visualize colocalization.

For *Aldh1l1*-eGFP immunofluorescence for astrocyte morphological analysis within the PFC and hippocampus, a staining protocol was adapted from a recently described paper [43]. Two sections per mouse were stained and used for image analysis. After washing and blocking steps, sections were incubated in chicken anti-GFP (1:800; Aves Labs Cat# GFP-1010). The next day, sections were incubated in 1:2000 Alexa Fluor 488 goat-anti chicken IgY (1:2000 dilution in PBST). Sections were then mounted and coverslipped in Fluoromount G. 40x (oil) images (layer II of the PFC and stratum radiatum region of the CA1) were acquired using a Leica SP8 confocal with the following parameters held constant for each condition (stress and control): 1024 x1024 scan format, 1 μm step size (bit depth of 12), 16-line average, 300 Hz scan speed, 1.0 AU pinhole, and 1.0 zoom. For analysis of astrocyte morphology, Imaris v9.1 (Bitplane) was utilized. Note that entire astrocytes were analyzed (i.e., partial astrocytes wherein somas were not within the z-stack range were not analyzed) [44]. Further, astrocytes chosen for analysis were clearly defined. An experimenter blind to conditions validated the criteria automated by Imaris. 3D surface rendering was then performed using the Imaris surface module. The selected astrocytes were then color-coded (in a heatmap fashion) according to the surface area of the entire astrocyte. The Imaris Filament module was also used to analyze astrocyte process length. Along these lines, the astrocytic branches were outlined using Autopath with starting point and seed point held constant between conditions (control and stress). Data were then extracted and input into Prism software for statistical analysis.

For connexin 30 and 43 staining, a similar immunofluorescence protocol was used as described above. After washing and blocking steps, sections (2 per mouse per region: hippocampus and PFC) were incubated in rabbit anti-connexin 30 (Invitrogen Cat 71-200; 1:1000 dilution in PBST) and mouse anti-connexin 43 (ThermoFisher Cat 13-8300; 1:500 dilution in PBST). Note that GFP primary antibody was not used to amplify the *Aldh1l1*-eGFP transgene signal in these sections. The following day, sections were washed and incubated in anti-mouse Cy5 (1:1000 dilution in PBST) and anti-rabbit Cy3 (1:1000 dilution in PBST). Sections were then washed and incubated in Hoechst (1:3000 dilution in PBST)

before being mounted and coverslipped. 40X oil z stack images were acquired on a Leica SP8 confocal using the following imaging parameters, which were held constant between stress condition: 1.0 zoom, 1.0 AU pinhole, 1024x1024 scan format, 200 Hz scan speed, 2 μm step size (bit depth of 12). All z-stack images were then imported into ImageJ for analysis of connexin 30/43 immunoreactive puncta per area.

Tissue processing for CUBIC tissue clearing

Control and stressed animals were injected with 8% chloral hydrate in 0.9% saline. Once anesthetized, transcardial perfusion was performed with a rate of flow ~3 mL/min. Note that animals were first perfused with PBS followed by a 4% PFA/PBS solution. Brains were then extracted, cut to ~2 mm thick sections using a mouse brain matrix, and finally post-fixed for ~9 hours in 4% PFA/PBS at 4 °C. Brains were covered and stored at 4 °C until CUBIC clearing was performed.

CUBIC tissue clearing, immunofluorescent staining, imaging, and analysis

CUBIC tissue clearing was adapted from methods previously described [28, 45–47]. To begin, 2 mm thick perfused coronal brain sections were cut to ~400 μm on a microtome. Sections were then incubated in CUBIC reagent-1 for two days at room temperature (covered; on a laboratory shaker/rocker). Brain slices were subsequently blocked in a solution containing 5% normal donkey serum (NDS) and 0.1% Triton X-100 in PBS for 1 day at room temperature. Next, sections were incubated in primary antibody (1:1000 anti-guinea pig NeuN Millipore Sigma, Cat # ABN90) for two days at room temperature in 10% NDS and 0.05% Triton X-100 in PBS. Brain slices were subsequently washed in PBS (3 washes; 3 hrs/wash) and incubated in secondary antibody (anti-guinea pig Cy5; 1:1000 dilution in 10% NDS, 0.05% Triton-X 100 PBS). Sections were then placed back into CUBIC reagent-1 for one day before imaging.

CUBIC images were acquired on a Leica SP8 confocal (~2 sections per mouse per region). The following imaging settings were held constant between stress condition: 10X magnification; 2.0 zoom; 1.0 AU pinhole; 512x512 scan format; 400 scan speed; 1 μm thick step size. Tissue was imaged to ~300 μm in depth.

Astrocyte cell density in control and UCMS CUBIC samples was analyzed using LASX software wherein the physical length (X, Y, and Z) was used to determine the volume of each ROI within the CUBIC-cleared image. The image was then imported into ImageJ, and the number of *Aldh1l1* eGFP positive cells was manually counted/tagged by an experimenter blind to stress condition to obtain a readout of astrocyte density per ROI volume. A similar protocol was performed in the acquired images to obtain neuronal cell density (NeuN positive cells were used to ascertain neuron density within the ROI volume).

For interastrocyte distance analysis, the pixel size for each image was first obtained using LASX software. Images were then imported into ImageJ, wherein a line was manually drawn between astrocytes and tagged. The length (i.e., distance) between astrocytes (analyzed from 30 cells per image) was recorded.

Finally, analysis of the number of nearest neighbors was performed in ImageJ. Reference cells were chosen (at least 25 stacks from the beginning of the image), and the number of neighboring astrocytes (within 25 μm from the reference cell) were tagged. Note that the number of nearest neighbors was calculated from three reference cells per image.

Electrophysiology

Brain slices were prepared as described previously [27]. Briefly, after anesthesia with 8% chloral hydrate in 0.9% NaCl, mouse brains were rapidly removed and placed into ice-cold oxygenated (95 % O_2/5 % CO_2) slice cutting aCSF with reduced Ca^{2+} and increased Mg^{2+} (in mM): 125 NaCl, 3.5 KCl, 25 $NaHCO_3$, 1.25 NaH_2PO_4, 0.1 $CaCl_2$, 3 $MgCl_2$ and 10 Glucose. Coronal brain slices (250 μm thickness) were cut at 4 °C with a Microslicer Zero 1N Vibratome (Ted Pella, Redding, CA) and transferred to oxygenated standard aCSF (in mM): 125 NaCl, 25 $NaHCO_3$, 1.25 NaH_2PO_4, 3.5 KCl, 2 $CaCl_2$, 1 $MgCl_2$ and 10 Glucose, osmolality, 295 ± 5 mOsm; pH 7.3–7.4). Slices recovered at room temperature for at least 1 hour.

Brain slice recordings were performed according to our previously published papers [28, 48, 49]. In brief, after recovering, coronal hippocampal and PFC slices (from both control and stressed mice) were placed in a recording chamber (RC-22; Warner Instruments) and were subsequently mounted on a BX51WI microscope (Olympus) which was equipped with infrared differential interference (IR-DIC). Slices were then perfused with oxygenated aCSF (2.0 mL/min) at room temperature. A fluorescent imaging system, Polychrome V system (Till Photonics, Germany) was used for high-resolution identification of $eGFP^+$ astrocytes.

Pipettes used for recording were fabricated from borosilicate capillaries (outer diameter: 1.5 mm, Warner Instrument, Hamden, CT) by utilizing a Flaming/Brown Micropipette Puller (Model P-97, Sutter Instrument). The recording electrodes had a resistance of 2-5 MΩ when filled with the electrode solution containing (in mM) 140 K-gluconate, 13.4 Na-gluconate, 0.5 $CaCl_2$, 1.0 $MgCl_2$, 5 EGTA, 10 HEPES, 3 Mg-ATP, and 0.3 Na-GTP (280 ± 5 mOsm, pH 7.25-7.27) [50, 51]. To record astrocyte syncytial isopotentiality, a Na^+- based electrode solution ($[Na^+]_P$) was made by equimolar substitution of K-gluconate with Na-gluconate. The pH was adjusted to 7.25-7.27 with NaOH.

Whole-cell patch clamp recordings were conducted with a MultiClamp 700B Amplifier and pClamp 9.2 software system (Molecular Devices, Sunnyvale, CA). A minimum 2 GΩ seal resistance was required before membrane rupture into the whole-cell configuration. Further, all electrophysiological experiments were performed at room temperature as per a prior study performed in our lab which examined gap junctional coupling strength [12]. The liquid junction potential was compensated for prior to forming the cell-attached mode for all recordings. The V_M was recorded under current-clamp mode for 5 min. The current profile was recorded under voltage clamp mode using 20 mV voltage steps from - 180 mV to + 20 mV for 25 ms recording duration. The rectification index (RI) was calculated by dividing the current amplitudes induced by + 20 mV (I_1) over - 180 mV (I_2). Recordings were discarded if the initial input resistance (R_{in}) was greater than 30 MΩ or varied greater than 10% during recording.

Statistics

Statistics were performed using GraphPad Prism 7.0 software, and data are presented as the mean ± SEM. However, as noted above, patch clamp recording data was analyzed using Clampfit 9.2 and OriginLab software. As stated in the figure legends, significance for experiments was set at $p < 0.05$ (*). Further, statistical comparisons between two groups were done using Student's t-tests, while comparisons between more than three groups/conditions/timepoints were done using an ANOVA. Post-hoc tests were conducted to show an interaction obtained from significant ANOVA results. Correlation analysis was conducted using Pearson Correlation Coefficient in Prism 7.0. Finally, Grubb's test was performed on each data set to assess whether statistically significant outliers were found in each group. Specifically, Grubb's test was used to exclude one control and one stressed animal from the open field test experiments (Fig. 1 and Fig. S1), and one control animal from the sucrose splash experiments (Fig. 1 and Fig. S1). Furthermore, for filament tracing and surface rendering analysis of astrocytes (Fig. 2), Grubb's test was used to exclude significant outliers for all cells obtained from each specific mouse before the average surface area and average process length was calculated from the hippocampus and PFC. Grubb's test was also used to exclude significant outliers of the V_M recording in patch-clamp data from each group.

Note that a 'Z-emotionality score' was calculated based upon the open field, tail suspension, and sucrose splash test results. This emotionality score was adapted from a previously published paper [52], and it was conducted because multiple behavioral testing paradigms in rodents may produce variability between testings. To do this, a Z-score was first determined for each parameter within each behavioral test using the following equation, wherein X refers to the data for the individual parameter within each test, μ refers to the mean for the control group, and σ refers to the standard deviation of the control group.

$$Z = (X - \mu)/\sigma$$

A Z-score for each behavioral test was then calculated by taking the average of each parameter for each paradigm, and the overall emotionality score was calculated by taking the average Z-score values across the behavioral tests.

Results

Expression of astrocytic Aldh1l1-eGFP transgene throughout the brain

To begin, we first confirmed that the *Aldh1l1*-eGFP transgene is expressed within the PFC and the hippocampus (two regions implicated in the etiology of depression) and that the transgene is specifically expressed within astrocytes. Indeed, serial sections acquired throughout the coronal aspect of the brain revealed the expression of the transgene in both noted regions (Fig. 1a). Further, co-labeling experiments with the neuronal marker NeuN and astrocytic marker GFAP revealed that the transgene is only found within astrocytes, and not neurons, as expected (Fig. 1b).

Six weeks of UCMS elicits depression-and anxiety-like behaviors in Aldh1l1-eGFP mice

To determine whether chronic stress influences astrocyte network anatomy and functionality, we turned to an unpredictable chronic mild stress (UCMS) paradigm that has been widely used in rodents to model depression [30–33] (Fig. 1c; Table I). Following the six-week UCMS paradigm, body weight and coat state in addition to depression and anxiety-like behaviors were measured. Like a previously published report [53], we found that our chronic stress paradigm led to a reduction in body weight gain across the six-week period (Fig. 1d). Specifically, we found a significant interaction between stress condition and body weight gain over time (Fig. 1d; $F_{(5, 125)} = 4.066$; $p = 0.0019$; Repeated Measures ANOVA). Post-hoc tests revealed a significant reduction in body weight in stressed animals at week 3, week 4, and week 6 (Fig. 1d; $p = 0.0001$, $p = 0.0223$, and $p = 0.0227$, respectively). Similarly, we found a significant increase in coat/fur state score (Fig. S1a) in UCMS mice (Fig. 1e; $F_{(5, 125)} = 12.45$; $p < 0.0001$; Repeated Measures ANOVA). Specifically, post hoc tests revealed a significant increase in coat score during weeks 3-6 (Fig. 1e; $p = 0.0122$ for week 3, $p < 0.0001$ for week 4, $p < 0.0001$ for week 5, and $p < 0.0001$ for week 6). Together, these data suggest that the UCMS paradigm leads to worsened fur state and a decrease in body weight gain.

Turning to the open field test, we found that chronic stress led to a decrease in the number of center entries in the arena (Fig. 1f; $t_{(24)} = 2.6265$; $p = 0.0148$; t-test) and the total time spent in the center of the arena (Fig. 1f; $t_{(24)} = 5.272$; $p < 0.0001$; t-test). Additionally, chronic stress led to a trending increase in the total time spent immobile in the tail suspension test (Fig. 1g; $t_{(25)} = 1.981$; $p = 0.0587$; t-test). The latency to first immobility was also decreased in stressed animals (Fig. 1g; $t_{(25)} = 2.069$; $p = 0.0491$; t-test). Finally, in the sucrose splash test, there was a trending, albeit non-significant, change in the number of grooming bouts in stressed mice (Fig. 1h; $t_{(21)} = 1.91$; $p = 0.0699$; t-test), and there was a significant decrease in the time spent grooming (Fig. 1h; $t_{(21)} = 3.078$; $p = 0.0057$; t-test).

The depressive-like behaviors in UCMS-exposed animals were also observed from analysis of z-scores within the respective paradigms. Specifically, we found a significant increase in the open field, tail suspension, and sucrose splash z-scores in stressed animals (Fig. S1b–S1d; $t_{(24)} = 4.017$; $p = 0.0005$; t-test for open field; $t_{(25)} = 2.247$; $p = 0.0337$; t-test for tail suspension; and $t_{(21)} = 2.702$; $p = 0.0134$; t-test for sucrose splash). Furthermore, the z-emotionality score (a readout of the combined behavioral results) (Fig. S1e) revealed a significant increase in stressed animals (Fig. S1f; $t_{(25)} = 4.798$); $p < 0.0001$; t-test). Taken together, these combined behavioral results reveal that our chronic stress paradigm was effective in eliciting depressive and anxiety-like behaviors.

UCMS leads to changes in astrocyte morphological complexity

To begin to profile changes in astrocyte anatomy after stress, we first asked whether individual astrocytes display morphological alterations after the chronic stress paradigm. To answer this question, we sacrificed control and stressed animals, collected hippocampal and PFC tissues, and immunolabeled for the *Aldh1l1*-eGFP transgene. We then conducted high magnification/high resolution confocal microscopy to map (in detail) changes within astrocyte process length and area (Fig. 2a–2b). Using filament tracing analysis, we found

that chronic stress led to a reduction in total astrocyte process length within both the hippocampus and the PFC (Fig. 2c1). Indeed, our analysis revealed that UCMS led to a significant shortening of astrocyte process length within the hippocampus (Fig. 2c1; $t_{(5)}$ = 3.844; p = 0.0121; t-test), and an even greater process shortening occurred in the PFC (Fig. 2c1; $t_{(9)}$ = 3.475; p = 0.0070; t-test).

We further explored the correlation between the shortening of astrocyte process length and Z-emotionality score. While the shortening of astrocyte process length was not significantly correlated to the Z-emotionality score in the hippocampus (Fig. 2c2; r = − 0.4323; p = 0.1663; one-tailed Pearson analysis), there was a correlation between astrocyte process length in the PFC and emotionality score (Fig. 2c2; r = −0.7124; p = 0.0069; one-tailed Pearson analysis). Turning to surface area analysis, we found a significant decrease in average astrocyte surface area in the hippocampus of chronically stressed animals (Fig. 2d1) (Fig. 2d1; $t_{(10)}$ = 4.433; p = 0.0013; t-test). Interestingly, while the process shortening was more severe in chronically stressed animals in the PFC, the average astrocyte surface area was not reduced (Fig. 2d1; $t_{(10)}$ = 1.02; p = 0.3316; t-test), indicating the regional heterogeneity in the pathological changes in astrocyte morphology. Additionally, within the hippocampus, a significant negative correlation was found between the average astrocyte surface area and Z-emotionality score (Fig. 2d2; r = −0.7707; p = 0.0017; one-tailed Pearson analysis); significance was not observed in the PFC (Fig. 2d2; r = −0.1733; p = 0.2951; one-tailed Pearson analysis). Taken together, these data suggest that at the *individual* cell level, the six-week chronic stress paradigm leads to heterogenous changes in astrocyte morphology in the mouse hippocampus and PFC but shortening of astrocyte processes appears to be a common pathological change in astrocytes.

UCMS does not alter astrocyte or neuron density, interastrocyte distance, or number of nearest neighbors within the hippocampus and PFC

Given the observed anatomical changes in *individual* astrocytes after chronic stress (Fig. 2), we next asked whether astrocyte *network* anatomy might be altered after chronic stress. Hence, control and UCMS mice were sacrificed via cardiac perfusion, and thick hippocampal (stratum radiatum) and PFC (layer II) brain slabs were collected. Tissue sections were then placed in CUBIC tissue clearing reagent and were subsequently imaged using confocal microscopy (Fig. 3a–3b). After imaging, astrocyte cell density, interastrocyte distance, and the number of nearest neighbors (Fig. 3c) were analyzed in both hippocampal and PFC sections. We first assessed whether astrocyte density is altered by UCMS (Fig. 3a–3d). Our analysis revealed that chronic stress did not change the density of astrocytes within either brain region (Fig. 3d; $t_{(12)}$ = 0.7034; p = 0.4953; t-test within the hippocampus and Fig. 3d; $t_{(11)}$ = 0.4409; p = 0.6679; t-test for PFC). Furthermore, we also immunolabeled for NeuN in our CUBIC (i.e., brain-cleared) sections (Fig. S2a–S2b). Our analysis of NeuN density revealed no significant difference in neuron density between control and stressed animals (Fig. S2c; $t_{(11)}$ = 0.1411; p = 0.8903; t-test for hippocampus and Fig. S2c; $t_{(10)}$ = 1.493; p = 0.1664; t-test for PFC). Together, these results suggest that neither astrocyte nor neuron density are altered by stress.

Interastrocyte distance was then measured as described in our recently published paper [26]. Along these lines, the distance was measured between neighboring astrocytes. Note that a randomly selected cell was used as the reference cell, and neighboring cells were defined as astrocytes that surrounded the reference cell (with no blood vessel in between) (Fig. 3c2). Our analysis of interastrocyte distance revealed no significant difference with respect to the distance between astrocytes from control and stressed animals (Fig. 3e; $t_{(12)} = 1.136$; $p = 0.2783$; t-test for hippocampus and Fig. 3e; $t_{(11)} = 1.042$; $p = 0.3198$; t-test for PFC).

Finally, our previously published papers found that within the murine hippocampus, interastrocytic electrical coupling and having at least 7-9 nearest neighbor (astrocytes) are key factors that underpin strong syncytial coupling [12, 28]. Given this, we were interested in determining whether chronic stress may alter the number of nearest neighboring astrocytes (Fig. 3c3). Interestingly, we found no significant difference between the number of nearest neighbors and stress condition (Fig. 3f; $t_{(12)} = 0.6384$; $p = 0.5352$; t-test for hippocampus and Fig. 3f; $t_{(11)} = 0.389$; $p = 0.7047$; t-test for PFC). Thus, six weeks of chronic stress does not appear to alter the number of nearest neighboring astrocytes.

UCMS does not alter astrocyte passive conductance

To determine whether chronic stress influences the functional K^+ channels, we first used $[K^+]_P$ to examine the resting membrane potential (V_M) and whole-cell astrocyte passive conductance as the readouts of changes in astrocyte K^+ channels conductance [54]. First, the dominant K^+ conductance over the Na^+ influx through non-selective cation channels (e.g., hemichannels and P2X7 receptors) and Na^+-dependent transporters creates P_{Na}/P_K of 0.015 [50]. Should stress reduce the expression of K^+ channels, one would anticipate an elevated P_{Na}/P_K ratio and therefore a depolarization in astrocyte V_M. We found no difference in the resting V_M between control and UCMS animals (Fig. S3a, $t = -0.934$; $p = 0.372$; unpaired t-test for hippocampus, and $t = -0.679$; $p = 0.513$; unpaired t-test for PFC), suggesting unaltered basal K^+ conductance after stress [55]. Further, the 'passive' nature of the membrane conductance has been shown to result from a combined expression of both known and unknown K^+ channels, such as the inwardly rectifying K^+ channel [56–59]. Should stress alter the composition of expressed K^+ channels, there would be an anticipated change in the linearity of passive conductance [54]. We found that the passive conductance was not affected by chronic stress in both the hippocampus and in the PFC, as shown by the current profile (Fig. S3b) and the linear *I-V* relationship (Fig. S3c). To further validate this notion, we analyzed the rectification index (RI) between control and stressed animals. The RI value close to 1 indicates nearly equal absolute values of outward and inward current under equivalent command of voltage, which is another characteristic of astrocyte passive conductance. We found comparable RI values between the control and UCMS group (Fig. S3d, $t = 1.062$; $p = 0.319$; unpaired t-test for hippocampus, and $t = -0.1049$; $p = 0.920$; unpaired t-test for PFC). It should be noted, however, that due to the low membrane resistance (R_M, 6.4 MΩ) and the resultant short length constant (3.6 μm) [54, 57], the passive conductance mostly reflects those channels activated around the tip of the recording electrode, with minor contributions from the distal processes and coupled neighboring astrocytes. Together, these data confirm that the passive membrane K^+ conductance of astrocytes is intact in chronically stressed mice.

UCMS leads to weakened astrocyte gap junction coupling

We next asked whether the anatomical differences in stressed animals (Fig. 2) may impair astrocyte syncytial isopotentiality within these limbic regions (i.e., hippocampus and PFC). To assess this, we used a K^+-free/Na^+ pipette solution to substitute the endogenous K^+ content in whole-cell recording which (in theory) should lead to a V_M depolarization (toward 0 mV) as anticipated from the Nernst equation. Notably, we have previously shown that the V_M (recorded with $[Na^+]_P$ from astrocytes remains at quasi-physiological conditions level at the steady-state ($V_{M, ss}$) [12, 28, 60]. This quasi-physiological $V_{M, ss}$ indicates the open state of the gap junctional coupling in an astrocyte network; disrupted syncytial coupling will lead to $V_{M, ss}$ shift toward 0 mV which indicates the closed state of a gap junction.

In $[Na^+]_P$ V_M recordings, the initial V_M ($V_{M, i}$) after the breaking-in into the whole-cell recordings is an indicator of an astrocyte's resting V_M, whereas the V_M at the steady-stated V_M ($V_{M, ss}$) informs the coupling strength of astrocyte network [12]. Consistent with the results from $[K^+]_P$ (Fig. S3a), the $V_{M, i}$ data revealed no significant differences between the groups (Fig. 4c; $t = -0.195$; $p = 0.847$; unpaired t-test for hippocampus, and $t = -0.955$; $p = 0.351$; unpaired t-test for PFC). However, the $V_{M, ss}$ in stressed animals shifted substantially toward the "closed" state of syncytial coupling compared to control animals (Fig. 4b, c). Within the hippocampus, the $V_{M, ss}$ in astrocytes recorded from the control group was −71.15 mV, while that of UMCS astrocytes was −66.31 mV, and statistical analysis revealed a significant difference between the readings (Fig. 4c; $t = -3.615$; $p = 0.0038$; unpaired t-test). The difference of $V_{M, ss}$ in the PFC in control, −76.96 mV and UCMS group, −71.28 mV was also significantly different (Fig. 4c; $t = -2.901$; $p = 0.0086$; unpaired t-test). Based on the shifts of $V_{M, ss}$ toward the closed state, there is an estimated 82.2% reduction in the syncytial coupling of astrocyte networks in the hippocampus [28]. Notably, the correlation between $V_{M, ss}$ and syncytial coupling was created from an astrocyte network in the hippocampus. Thus, the calculation of syncytial coupling reduction was not feasible in the PFC due to the different baseline $V_{M, ss}$ in the PFC compared to the hippocampus.

Note that in the control group, the $V_{M, ss}$ recorded from PFC astrocytes is closer to the physiological $V_{M, i}$ than hippocampal astrocytes, indicating PFC astrocytes have a stronger coupling strength than hippocampal astrocytes (Fig. 4e and f, right). These results are consistent with our previous finding that astrocytes in certain cortical areas showed stronger syncytial coupling than in the hippocampus [28]. Taken together, these data suggest that six weeks of stress leads to a reduction in syncytial coupling strength of astrocytes in both the hippocampus and the PFC. It should be noted that it is still unknown at this point whether there is sex-dependent difference in stress-induced impairment of syncytial coupling. This question certainly warrants full-scale study in the future.

UCMS impairs the K^+ redistribution capacity of an astrocyte syncytium

One key role of astrocytes is the clearance of K^+ from the extracellular space after periods of neuronal activity [61–63]. Indeed, the K^+ spatial buffering hypothesis posits that K^+ ions must be relocated across gap junctions to areas of the brain with less neural activity [17, 64]. Hence, a high permeability to K^+ and a strong capacity to redistribute K^+ ions

are necessary for astrocytes' syncytial function. Given the observed reduction in syncytial coupling strength (Fig. 4), we predicted that chronic stress would also impair the K^+ spatial redistribution capacity of astrocytes. To assess this hypothesis, we utilized our $[Na^+]_P$ to create a 'K^+ deficient astrocyte' inside a syncytium. By experimentally uptake a controlled amount of K^+ ions, the efficiency of a coupled syncytium to dissipate the accumulated K^+ ions can be calculated [57]. Experimentally, a series of inward current pulses with increased duration was applied to a $[Na^+]_P$ recorded astrocyte in a syncytium (Fig. 5a). The step duration-dependent increase in $[K^+]_i$ is reflected by the negative shift in V_{rev} values at the end of the negative holding current in each step (dots in Fig. 5b). ΔV_M was calculated from V_{rev} subtracted from the V_M before the negative holding current. As demonstrated in our previous publications, the smaller the absolute value of ΔV_M, the stronger the capacity of the syncytium to dissipate the accumulated K^+ content in the recorded astrocyte to the coupled syncytium [27, 48]. In other words, the larger absolute values of ΔV_M indicate weakened K^+ redistribution capacity, or syncytial coupling [48, 57]. This occurred in the astrocyte syncytia after UCMS in the hippocampus (Fig. 5b–c, n = 13 for control and n = 12 for UCMS, Two-Way Mixed-Design ANOVA) but not to the PFC (Fig. 5d, n = 6 for control and n = 7 for UCMS, Two-Way Mixed-Design ANOVA). These results are consistent with a more severe impairment of syncytial coupling observed in the hippocampal astrocyte syncytial network compared to the PFC network (Fig. 4b–f). Additionally, these results also reiterate that the strength of syncytial coupling in the PFC is stronger than the hippocampus, making the PFC more 'resilient' to a 6-week UCMS paradigm. Altogether, these results show that six weeks of chronic stress impairs the K^+ redistribution capacity of the astrocyte network in the hippocampus but not the PFC.

UCMS does not alter the number of connexin 30/43 immunoreactive puncta within the hippocampus or PFC

A recent study showed that reduction of astrocytic connexin (Cx) 43 and 30 is sufficient to disrupt syncytial coupling [65]. To explore if this could also contribute, in part, to the disrupted syncytial coupling, we next tested whether the expression of Cx43 and Cx30 - two of the major proteins that from gap junctions [66] - could be altered by chronic stress. To this end, control and UCMS-exposed animals were sacrificed, and hippocampal and PFC brain sections were collected and stained for Cx30 and Cx43 expression (Fig. 6a–6b). Analysis of connexin 30 puncta revealed no significant difference in immunoreactivity in either the hippocampus or the PFC after stress (Fig. 6c; $t_{(10)} = 0.8296$; $p = 0.4261$ for hippocampus and $t_{(10)} = 0.8638$; $p = 0.4079$ for PFC; t-tests). Similarly, no change was observed with respect to Cx43 puncta immunoreactivity in either the hippocampus or the PFC (Fig. 6d; $t_{(10)} = 0.2755$; $p = 0.7886$ for hippocampus and $t_{(10)} = 1.275$; $p = 0.2313$ for PFC; t-tests). Together, these results suggest that Cx30 and Cx43 total protein levels are not altered by our UCMS paradigm.

Discussion

Here, we expand upon previous studies - providing data showing that astrocyte morphology is altered by chronic stress. In addition to morphological changes observed at the individual

cell level, we also show that astrocyte network anatomy and syncytial coupling strength are altered in a mouse model of depression.

High magnification/resolution confocal imaging revealed that our six-week UCMS paradigm led to a marked reduction in total astrocyte process length and surface area (Fig. 2), without changing the total number of astrocytes (or neurons) (Fig. 3 and Fig. S2). These findings are in line with a previous study that used chronic stress paradigms to profile cortical astrocytes [20, 22]. Additionally, we were able to correlate these two morphological readouts (process length and surface area) with the emotionality score of each experimental animal. Here, we should note that while we only examined the stratum radiatum and PFC (layer II) in our study, the astrocytic process atrophy that we observed in these regions (which appears similar to previously reported age-dependent decreases in astrocyte processes [67–69] is likely to be circuit specific. Indeed, the study performed by Tynan et al. found no evidence of astrocytic atrophy within the motor cortex [23] - a region that is not typically thought to be especially significant in the etiology of mood-related disorders.

With respect to understanding the implications of the individual astrocyte morphological changes observed after stress, here it should be mentioned that extensive dendritic atrophy (and dendritic spine loss) has been observed within the PFC after chronic stress [70–72]. Paralleling these animal studies, human imaging studies have also reported significant reductions in the volume of grey matter within the PFC in patients with a history of depression [73, 74]. Hence, while neuronal alterations/dysfunction may be a key contributor in the etiology of mood-related disorders, the precise mechanism(s) that underpin these changes are not yet known. The fact that astrocytes (within these same brain regions) also show atrophy of their processes, coupled with emerging evidence suggesting that astrocytes are key players in controlling synapse formation and function [75], and that astrocytes closely associate with synapses [76–78] raises the prospect that astrocytes may actually be initiating neuronal/synaptic dysfunction when mood disorders first arise. Given this, studies that examine whether astrocyte dysfunction proceeds (and hence significantly contributes to) neuronal dysfunction during chronic stress, are of high merit.

Turning to network-level profiling, to our knowledge, we are the first to report that astrocyte syncytial anatomy remains intact after chronic stress. Indeed, we observed no differences in interastrocyte distance (i.e., the distance between two neighboring astrocytes), in both the PFC and in the hippocampus after chronic stress (Fig. 3). At first glance, one may postulate that the lack of difference in astrocyte density and interastrocyte distance may make for no difference in the strength of astrocyte network coupling. However, it is important to note that under baseline conditions (i.e., no stress), in our previously published report, we did not observe a definitive correlation between syncytial anatomy and strength of syncytial isopotentiality [28]. As such, caution should be taken when positing that no difference in astrocyte density and/or interastrocyte distance means that no change in coupling strength will be observed using our novel electrophysiological K^+-free/Na^+-containing recording pipette solution [12].

Along these lines, our electrophysiological recordings showed a weakening in syncytial coupling strength in stressed mice (Fig. 4). Using this innovative technique, which serves

to create a ‘reporter astrocyte’ that can provide a readout of network coupling [12, 28], our results suggest that not only *individual* astrocyte anatomy/morphology, but also *network* level coupling is impaired by chronic stress. Notably, we only profiled hippocampal and PFC subregions in our recording experiments (paralleling our morphological data). It would be interesting to test whether other mood-related regions - such as the habenula, amygdala, and nucleus accumbens - regions known to be involved in the etiology of depression-like behaviors and/or altered by stress [79–82] - show similar impairments in response to stress. Furthermore, whether this weakened coupling strength is specific to limbic circuits remains to be determined.

Given our observations that network-level anatomical and electrophysiological differences were observed after stress and that vertebrate gap junctions are comprised of connexin proteins [66], we were somewhat surprised that our analysis did not reveal any effect of stress on connexin 30/43 immunoreactive puncta density (Fig. 6). Though we did not include a Western Blot experiment in parallel with our immunofluorescent data, these results are in conflict with results from a recently published paper that found a reduction in the density of connexin 30 and 43 positive puncta in the cortex in rats exposed to a chronic stress paradigm [83]. While the differential results between our study and those published by Miguel-Hidalgo et al. may be attributed to differences in species and/or brain region analyzed, another study found that acute stress induces the opening of connexin 43 channels within astrocytes and that this opening is potentiated by chronic stress [84]. Furthermore, connexins not only form intercellular gap junctions, but those that are unpaired may also form hemichannels [85]. Thus, the regulation of gap junction coupling by connexins is likely quite complex.

Another potential mechanism for our result showing no change in connexin expression in control and UCMS astrocytes is presented in our summary schematic (Fig. 7). Given our results that UCMS astrocytic processes show atrophy (Fig. 2), connexins from neighboring astrocytes may not be able to properly dock to form a gap junction. Such a model would not depend on connexin expression differences in control versus UCMS astrocytes, but rather localization. Hence, there may be more ‘de-docked’ gap junctions in UCMS astrocytes relative to control astrocytes. This mechanism would also support our observation of weakened gap junction coupling strength in astrocytes from UCMS mice (described below). Transmission electron microscopy may be worthwhile to determine whether interastrocyte connexin docking is altered by stress [66]. In summary, astrocyte coupling can be disrupted at the molecular, cellular, and/or syncytial levels via alterations in the open probability of gap junctions, a decrease in the number of gap junctions, and/or de-docking of gap junctions (due to atrophy of astrocytes), as we hypothesize (Fig. 7).

Our current study did not investigate the mechanism(s) underlying the weakened gap junction coupling observed after chronic stress, or the functional ramifications of this weakened coupling on interastrocyte communication. However, placed within a mechanistic model, alterations in calcium signaling within the astrocyte network may be one of the possible mechanisms [86, 87]. No study (to the best of our knowledge) has examined whether chronic stress alters both spontaneous and/or evoked calcium events within astrocyte microdomains. However, a recently published study demonstrated that acute stress

leads to astrocyte atrophy and prolongs spontaneous calcium events within astrocytes [25]. Interestingly, one of the key features of astrocytes is their intricate morphology and their ability to respond to stimuli (endogenous or exogenous) to generate calcium increases that subsequently couple to downstream cellular signaling processes to regulate animal physiology and behavior [88, 89]. Hence, this calls into question the idea that calcium may serve as a potential regulator of astrocyte syncytial isopotentiality in both healthy and diseased states - a topic that is currently under investigation in our lab. Indeed, it is important to note the intricate morphology of astrocytes. Several electron microscopy studies have revealed that fine, terminal (i.e. 'leaflet') astrocytic processes are devoid of larger organelles such as ER and mitochondria [78, 90–92]. Should the atrophy in astrocytes from chronically stressed mice mainly result from the withdrawal of small leaflets, one would not anticipate an overall reduction in astrocyte calcium activity but may expect to observe a reduced inter-astrocytic calcium signal. However, if astrocyte atrophy also occurs in larger ER/mitochondria-containing astrocyte processes, then one may observe an overall reduction in calcium activity. Future studies that examine astrocytic calcium signaling after chronic stress - and how such signaling may regulate the state of syncytial coupling - are of high merit.

In total, these studies reveal that a six-week UCMS paradigm alters not only astrocyte morphology, but also astrocyte network coupling. These observations suggest that other neuropsychiatric conditions may change the spatial organization of the astrocyte network and alter coupling strength. Hence, our study reveals important insights related to how depression disrupts astrocyte network communication.

Supplementary Material

Refer to Web version on PubMed Central for supplementary material.

Acknowledgements

The authors thank Michaela Witt for technical assistance.

Funding and Disclosure

This work was sponsored by a grant from National Institute of Neurological Disorders and Stroke; Grant code: RO1NS116059 (MZ), and an Alumni Grants for Graduate Research and Scholarship (AGGRS) and Distinguished University Fellowship, Ohio State University (to SA).

Data Availability

All data generated or analyzed for this study are included in this article. Please contact the corresponding author with questions or requests.

References

1. Hasin DS, Sarvet AL, Meyers JL, Saha TD, Ruan WJ, Stohl M, Grant BF (2018) Epidemiology of Adult DSM-5 Major Depressive Disorder and Its Specifiers in the United States. JAMA Psychiatry 75:336–346 [PubMed: 29450462]
2. Friedrich MJ (2017) Depression Is the Leading Cause of Disability Around the World. JAMA 317:1517

3. Hammen C (2005) Stress and depression. Annu Rev Clin Psychol 1:293–319 [PubMed: 17716090]
4. Yang L, Zhao Y, Wang Y, Liu L, Zhang X, Li B, Cui R (2015) The Effects of Psychological Stress on Depression. Curr Neuropharmacol 13:494–504 [PubMed: 26412069]
5. Duman RS (2009) Neuronal damage and protection in the pathophysiology and treatment of psychiatric illness: stress and depression. Dialogues Clin Neurosci 11:239–255 [PubMed: 19877493]
6. Duman RS, Aghajanian GK (2012) Synaptic dysfunction in depression: potential therapeutic targets. Science 338:68–72 [PubMed: 23042884]
7. Liu W, Ge T, Leng Y, Pan Z, Fan J, Yang W, Cui R (2017) The Role of Neural Plasticity in Depression: From Hippocampus to Prefrontal Cortex. Neural Plast 2017:6871089 [PubMed: 28246558]
8. Bennett MV, Contreras JE, Bukauskas FF, Saez JC (2003) New roles for astrocytes: gap junction hemichannels have something to communicate. Trends Neurosci 26:610–617 [PubMed: 14585601]
9. Giaume C, McCarthy KD (1996) Control of gap-junctional communication in astrocytic networks. Trends Neurosci 19:319–325 [PubMed: 8843600]
10. Dermietzel R, Spray DC (1993) Gap junctions in the brain: where, what type, how many and why? Trends Neurosci 16:186–192 [PubMed: 7685944]
11. Kiyoshi CM, Zhou M (2019) Astrocyte syncytium: a functional reticular system in the brain. Neural regeneration research 14:595–596 [PubMed: 30632498]
12. Ma B, Buckalew R, Du Y, Kiyoshi CM, Alford CC, Wang W, McTigue DM, Enyeart JJ, Terman D, Zhou M (2016) Gap junction coupling confers isopotentiality on astrocyte syncytium. Glia 64:214–226 [PubMed: 26435164]
13. Kuga N, Sasaki T, Takahara Y, Matsuki N, Ikegaya Y (2011) Large-scale calcium waves traveling through astrocytic networks in vivo. J Neurosci 31:2607–2614 [PubMed: 21325528]
14. Langer J, Stephan J, Theis M, Rose CR (2012) Gap junctions mediate intercellular spread of sodium between hippocampal astrocytes in situ. Glia 60:239–252 [PubMed: 22025386]
15. Lin JH, Weigel H, Cotrina ML, Liu S, Bueno E, Hansen AJ, Hansen TW, Goldman S, Nedergaard M (1998) Gap-junction-mediated propagation and amplification of cell injury. Nat Neurosci 1:494–500 [PubMed: 10196547]
16. Newman EA (2001) Propagation of intercellular calcium waves in retinal astrocytes and Muller cells. J Neurosci 21:2215–2223 [PubMed: 11264297]
17. Orkand RK, Nicholls JG, Kuffler SW (1966) Effect of nerve impulses on the membrane potential of glial cells in the central nervous system of amphibia. J Neurophysiol 29:788–806 [PubMed: 5966435]
18. Rose CR, Ransom BR (1997) Gap junctions equalize intracellular Na+ concentration in astrocytes. Glia 20:299–307 [PubMed: 9262234]
19. Rouach N, Koulakoff A, Abudara V, Willecke K, Giaume C (2008) Astroglial metabolic networks sustain hippocampal synaptic transmission. Science 322:1551–1555 [PubMed: 19056987]
20. Simard S, Coppola G, Rudyk CA, Hayley S, McQuaid RJ, Salmaso N (2018) Profiling changes in cortical astroglial cells following chronic stress. Neuropsychopharmacology 43:1961–1971 [PubMed: 29907879]
21. Wang F, Smith NA, Xu Q, Fujita T, Baba A, Matsuda T, Takano T, Bekar L, Nedergaard M (2012) Astrocytes modulate neural network activity by Ca(2)+-dependent uptake of extracellular K+. Science signaling 5:ra26 [PubMed: 22472648]
22. Naskar S, Chattarji S (2019) Stress Elicits Contrasting Effects on the Structure and Number of Astrocytes in the Amygdala versus Hippocampus. eNeuro 6
23. Tynan RJ, Beynon SB, Hinwood M, Johnson SJ, Nilsson M, Woods JJ, Walker FR (2013) Chronic stress-induced disruption of the astrocyte network is driven by structural atrophy and not loss of astrocytes. Acta Neuropathol 126:75–91 [PubMed: 23512378]
24. Walker R, Tynan R, Beyon S, Nilsson M (2013) 70. Chronic stress induces profound structural atrophy of astrocytes within the prefrontal cortex: An emerging story in glial remodeling in response to stress. Brain Behav Immun 32:e20–e21

25. Murphy-Royal C, Johnston AD, Boyce AKJ, Diaz-Castro B, Institoris A, Peringod G, Zhang O, Stout RF, Spray DC, Thompson RJ, Khakh BS, Bains JS, Gordon GR (2020) Stress gates an astrocytic energy reservoir to impair synaptic plasticity. Nature communications 11:2014
26. Stephan J, Eitelmann S, Zhou M (2021) Approaches to Study Gap Junctional Coupling. Front Cell Neurosci 15:640406 [PubMed: 33776652]
27. Zhong S, Du Y, Kiyoshi CM, Ma B, Alford CC, Wang Q, Yang Y, Liu X, Zhou M (2016) Electrophysiological behavior of neonatal astrocytes in hippocampal stratum radiatum. Molecular brain 9:34 [PubMed: 27004553]
28. Kiyoshi CM, Du Y, Zhong S, Wang W, Taylor AT, Xiong B, Ma B, Terman D, Zhou M (2018) Syncytial isopotentiality: A system-wide electrical feature of astrocytic networks in the brain. Glia 66:2756–2769 [PubMed: 30277621]
29. Yang Y, Vidensky S, Jin L, Jie C, Lorenzini I, Frankl M, Rothstein JD (2011) Molecular comparison of GLT1+ and ALDH1L1+ astrocytes in vivo in astroglial reporter mice. Glia 59:200–207 [PubMed: 21046559]
30. Logan RW, Edgar N, Gillman AG, Hoffman D, Zhu X, McClung CA (2015) Chronic Stress Induces Brain Region-Specific Alterations of Molecular Rhythms that Correlate with Depression-like Behavior in Mice. Biol Psychiatry 78:249–258 [PubMed: 25771506]
31. Monteiro S, Roque S, de Sa-Calcada D, Sousa N, Correia-Neves M, Cerqueira JJ (2015) An efficient chronic unpredictable stress protocol to induce stress-related responses in C57BL/6 mice. Front Psychiatry 6:6 [PubMed: 25698978]
32. Willner P (1997) Validity, reliability and utility of the chronic mild stress model of depression: a 10-year review and evaluation. Psychopharmacology 134:319–329
33. Li N, Liu RJ, Dwyer JM, Banasr M, Lee B, Son H, Li XY, Aghajanian G, Duman RS (2011) Glutamate N-methyl-D-aspartate receptor antagonists rapidly reverse behavioral and synaptic deficits caused by chronic stress exposure. Biol Psychiatry 69:754–761 [PubMed: 21292242]
34. Frisbee JC, Brooks SD, Stanley SC, d'Audiffret AC (2015) An Unpredictable Chronic Mild Stress Protocol for Instigating Depressive Symptoms, Behavioral Changes and Negative Health Outcomes in Rodents. Journal of visualized experiments : JoVE
35. Dominguez G, Henkous N, Prevot T, David V, Guillou JL, Belzung C, Mons N, Beracochea D (2019) Sustained corticosterone rise in the prefrontal cortex is a key factor for chronic stress-induced working memory deficits in mice. Neurobiol Stress 10:100161 [PubMed: 31309134]
36. Nguyen ET, Selmanovic D, Maltry M, Morano R, Franco-Villanueva A, Estrada CM, Solomon MB (2020) Endocrine stress responsivity and social memory in 3xTg-AD female and male mice: A tale of two experiments. Horm Behav 126:104852 [PubMed: 32949555]
37. Aten S, Page CE, Kalidindi A, Wheaton K, Niraula A, Godbout JP, Hoyt KR, Obrietan K (2019) miR-132/212 is induced by stress and its dysregulation triggers anxiety-related behavior. Neuropharmacology 144:256–270 [PubMed: 30342060]
38. Cryan JF, Mombereau C, Vassout A (2005) The tail suspension test as a model for assessing antidepressant activity: review of pharmacological and genetic studies in mice. Neurosci Biobehav Rev 29:571–625 [PubMed: 15890404]
39. Isingrini E, Camus V, Le Guisquet AM, Pingaud M, Devers S, Belzung C (2010) Association between repeated unpredictable chronic mild stress (UCMS) procedures with a high fat diet: a model of fluoxetine resistance in mice. PLoS One 5:e10404 [PubMed: 20436931]
40. Aten S, Kalidindi A, Yoon H, Rumbaugh G, Hoyt KR, Obrietan K (2021) SynGAP is expressed in the murine suprachiasmatic nucleus and regulates circadian-gated locomotor activity and light-entrainment capacity. Eur J Neurosci 53:732–749 [PubMed: 33174316]
41. Aten S, Hansen KF, Price KH, Wheaton K, Kalidindi A, Garcia A, Alzate-Correa D, Hoyt KR, Obrietan K (2018) miR-132 couples the circadian clock to daily rhythms of neuronal plasticity and cognition. Learn Mem 25:214–229 [PubMed: 29661834]
42. Aten S, Page CE, Kalidindi A, Wheaton KL, Niraula A, Godbout JP, Hoyt KR, Obrietan K (2018) Data highlighting the expression of two miR-132/212 target genes-Sirt1 and Pten-after chronic stress. Data Brief 21:2323–2329 [PubMed: 30555870]

43. Huang AY, Woo J, Sardar D, Lozzi B, Bosquez Huerta NA, Lin CJ, Felice D, Jain A, Paulucci-Holthauzen A, Deneen B (2020) Region-Specific Transcriptional Control of Astrocyte Function Oversees Local Circuit Activities. Neuron 106:992–1008 e1009 [PubMed: 32320644]
44. Lanjakornsiripan D, Pior BJ, Kawaguchi D, Furutachi S, Tahara T, Katsuyama Y, Suzuki Y, Fukazawa Y, Gotoh Y (2018) Layer-specific morphological and molecular differences in neocortical astrocytes and their dependence on neuronal layers. Nature communications 9:1623
45. Susaki EA, Tainaka K, Perrin D, Yukinaga H, Kuno A, Ueda HR (2015) Advanced CUBIC protocols for whole-brain and whole-body clearing and imaging. Nature protocols 10:1709–1727 [PubMed: 26448360]
46. Susaki EA, Tainaka K, Perrin D, Kishino F, Tawara T, Watanabe TM, Yokoyama C, Onoe H, Eguchi M, Yamaguchi S, Abe T, Kiyonari H, Shimizu Y, Miyawaki A, Yokota H, Ueda HR (2014) Whole-brain imaging with single-cell resolution using chemical cocktails and computational analysis. Cell 157:726–739 [PubMed: 24746791]
47. Tainaka K, Kubota SI, Suyama TQ, Susaki EA, Perrin D, Ukai-Tadenuma M, Ukai H, Ueda HR (2014) Whole-body imaging with single-cell resolution by tissue decolorization. Cell 159:911–924 [PubMed: 25417165]
48. Wang Q, Wang W, Aten S, Kiyoshi CM, Du Y, Zhou M (2020) Epileptiform Neuronal Discharges Impair Astrocyte Syncytial Isopotentiality in Acute Hippocampal Slices. Brain Sci 10 [PubMed: 33374858]
49. Du Y, Wang W, Lutton AD, Kiyoshi CM, Ma B, Taylor AT, Olesik JW, McTigue DM, Askwith CC, Zhou M (2018) Dissipation of transmembrane potassium gradient is the main cause of cerebral ischemia-induced depolarization in astrocytes and neurons. Exp Neurol 303:1–11 [PubMed: 29407729]
50. Stephan J, Haack N, Kafitz KW, Durry S, Koch D, Hochstrate P, Seifert G, Steinhauser C, Rose CR (2012) Kir4.1 channels mediate a depolarization of hippocampal astrocytes under hyperammonemic conditions in situ. Glia 60:965–978 [PubMed: 22431254]
51. Ma BF, Xie MJ, Zhou M (2012) Bicarbonate efflux via GABA(A) receptors depolarizes membrane potential and inhibits two-pore domain potassium channels of astrocytes in rat hippocampal slices. Glia 60:1761–1772 [PubMed: 22855415]
52. Shepard R, Page CE, Coutellier L (2016) Sensitivity of the prefrontal GABAergic system to chronic stress in male and female mice: Relevance for sex differences in stress-related disorders. Neuroscience 332:1–12 [PubMed: 27365172]
53. Zhu S, Wang J, Zhang Y, Li V, Kong J, He J, Li XM (2014) Unpredictable chronic mild stress induces anxiety and depression-like behaviors and inactivates AMP-activated protein kinase in mice. Brain Res 1576:81–90 [PubMed: 24971831]
54. Zhou M, Du Y, Aten S, Terman D (2021) On the electrical passivity of astrocyte potassium conductance. J Neurophysiol 126:1403–1419 [PubMed: 34525325]
55. Dallerac G, Chever O, Rouach N (2013) How do astrocytes shape synaptic transmission? Insights from electrophysiology. Front Cell Neurosci 7:159 [PubMed: 24101894]
56. Du Y, Kiyoshi CM, Wang Q, Wang W, Ma B, Alford CC, Zhong S, Wan Q, Chen H, Lloyd EE, Bryan RM (2016) Genetic deletion of TREK-1 or TWIK-1/TREK-1 potassium channels does not alter the basic electrophysiological properties of mature hippocampal astrocytes in situ. Front Cell Neurosci doi: 10.3389/fncel.2016.00013
57. Du Y, Ma B, Kiyoshi CM, Alford CC, Wang W, Zhou M (2015) Freshly dissociated mature hippocampal astrocytes exhibit passive membrane conductance and low membrane resistance similarly to syncytial coupled astrocytes. J Neurophysiol 113:3744–3750 [PubMed: 25810481]
58. Ma B, Xu G, Wang W, Enyeart JJ, Zhou M (2014) Dual patch voltage clamp study of low membrane resistance astrocytes in situ. Molecular brain 7:18 [PubMed: 24636341]
59. Zhou M, Kimelberg HK (2000) Freshly isolated astrocytes from rat hippocampus show two distinct current patterns and different [K(+)](o) uptake capabilities. J Neurophysiol 84:2746–2757 [PubMed: 11110805]
60. Huang M, Du Y, Kiyoshi CM, Wu X, Askwith CC, McTigue DM, Zhou M (2018) Syncytial Isopotentiality: An Electrical Feature of Spinal Cord Astrocyte Networks. Neuroglia 1:271–279

61. Ballanyi K, Grafe P, ten Bruggencate G (1987) Ion activities and potassium uptake mechanisms of glial cells in guinea-pig olfactory cortex slices. J Physiol 382:159–174 [PubMed: 2442359]
62. Hertz L (1965) Possible role of neuroglia: a potassium-mediated neuronal--neuroglial--neuronal impulse transmission system. Nature 206:1091–1094 [PubMed: 5325441]
63. Newman EA, Frambach DA, Odette LL (1984) Control of extracellular potassium levels by retinal glial cell K+ siphoning. Science 225:1174–1175 [PubMed: 6474173]
64. Kofuji P, Newman EA (2004) Potassium buffering in the central nervous system. Neuroscience 129:1045–1056 [PubMed: 15561419]
65. Du Y, Brennan FH, Popovich PG, Zhou M (2022) Microglia maintain the normal structure and function of the hippocampal astrocyte network. Glia 70:1359–1379 [PubMed: 35394085]
66. Nielsen MS, Axelsen LN, Sorgen PL, Verma V, Delmar M, Holstein-Rathlou NH (2012) Gap junctions. Compr Physiol 2:1981–2035 [PubMed: 23723031]
67. Verkhratsky A, Lazareva N, Semyanov A (2022) Glial decline and loss of homeostatic support rather than inflammation defines cognitive aging. Neural regeneration research 17:565–566 [PubMed: 34380892]
68. Popov A, Brazhe A, Denisov P, Sutyagina O, Li L, Lazareva N, Verkhratsky A, Semyanov A (2021) Astrocyte dystrophy in ageing brain parallels impaired synaptic plasticity. Aging Cell 20:e13334 [PubMed: 33675569]
69. Verkhratsky A, Augusto-Oliveira M, Pivoriunas A, Popov A, Brazhe A, Semyanov A (2021) Astroglial asthenia and loss of function, rather than reactivity, contribute to the ageing of the brain. Pflugers Arch 473:753–774 [PubMed: 32979108]
70. Izquierdo A, Wellman CL, Holmes A (2006) Brief uncontrollable stress causes dendritic retraction in infralimbic cortex and resistance to fear extinction in mice. J Neurosci 26:5733–5738 [PubMed: 16723530]
71. Radley JJ, Sisti HM, Hao J, Rocher AB, McCall T, Hof PR, McEwen BS, Morrison JH (2004) Chronic behavioral stress induces apical dendritic reorganization in pyramidal neurons of the medial prefrontal cortex. Neuroscience 125:1–6 [PubMed: 15051139]
72. Shansky RM, Hamo C, Hof PR, McEwen BS, Morrison JH (2009) Stress-induced dendritic remodeling in the prefrontal cortex is circuit specific. Cereb Cortex 19:2479–2484 [PubMed: 19193712]
73. Drevets WC, Price JL, Simpson JR Jr., Todd RD, Reich, Vannier M, Raichle ME (1997) Subgenual prefrontal cortex abnormalities in mood disorders. Nature 386:824–827 [PubMed: 9126739]
74. Hastings RS, Parsey RV, Oquendo MA, Arango V, Mann JJ (2004) Volumetric analysis of the prefrontal cortex, amygdala, and hippocampus in major depression. Neuropsychopharmacology 29:952–959 [PubMed: 14997169]
75. Chung WS, Allen NJ, Eroglu C (2015) Astrocytes Control Synapse Formation, Function, and Elimination. Cold Spring Harbor perspectives in biology 7:a020370 [PubMed: 25663667]
76. Ventura R, Harris KM (1999) Three-dimensional relationships between hippocampal synapses and astrocytes. J Neurosci 19:6897–6906 [PubMed: 10436047]
77. Semyanov A, Verkhratsky A (2021) Astrocytic processes: from tripartite synapses to the active milieu. Trends Neurosci 44:781–792 [PubMed: 34479758]
78. Aten S, Kiyoshi CM, Arzola EP, Patterson JA, Taylor AT, Du Y, Guiher AM, Philip M, Camacho EG, Mediratta D, Collins K, Boni K, Garcia SA, Kumar R, Drake AN, Hegazi A, Trank L, Benson E, Kidd G, Terman D, Zhou M (2022) Ultrastructural view of astrocyte arborization, astrocyte-astrocyte and astrocyte-synapse contacts, intracellular vesicle-like structures, and mitochondrial network. Prog Neurobiol 213:102264 [PubMed: 35283239]
79. Browne CA, Hammack R, Lucki I (2018) Dysregulation of the Lateral Habenula in Major Depressive Disorder. Front Synaptic Neurosci 10:46 [PubMed: 30581384]
80. Campioni MR, Xu M, McGehee DS (2009) Stress-induced changes in nucleus accumbens glutamate synaptic plasticity. J Neurophysiol 101:3192–3198 [PubMed: 19357347]
81. Zhang X, Ge TT, Yin G, Cui R, Zhao G, Yang W (2018) Stress-Induced Functional Alterations in Amygdala: Implications for Neuropsychiatric Diseases. Frontiers in neuroscience 12:367 [PubMed: 29896088]

82. Cerniauskas I, Winterer J, de Jong JW, Lukacsovich D, Yang H, Khan F, Peck JR, Obayashi SK, Lilascharoen V, Lim BK, Foldy C, Lammel S (2019) Chronic Stress Induces Activity, Synaptic, and Transcriptional Remodeling of the Lateral Habenula Associated with Deficits in Motivated Behaviors. Neuron 104:899–915 e898 [PubMed: 31672263]

83. Miguel-Hidalgo JJ, Moulana M, Deloach PH, Rajkowska G (2018) Chronic Unpredictable Stress Reduces Immunostaining for Connexins 43 and 30 and Myelin Basic Protein in the Rat Prelimbic and Orbitofrontal Cortices. Chronic Stress (Thousand Oaks) 2

84. Orellana JA, Moraga-Amaro R, Diaz-Galarce R, Rojas S, Maturana CJ, Stehberg J, Saez JC (2015) Restraint stress increases hemichannel activity in hippocampal glial cells and neurons. Front Cell Neurosci 9:102 [PubMed: 25883550]

85. Saez JC, Berthoud VM, Branes MC, Martinez AD, Beyer EC (2003) Plasma membrane channels formed by connexins: their regulation and functions. Physiol Rev 83:1359–1400 [PubMed: 14506308]

86. Verkhratsky A (2006) Glial calcium signaling in physiology and pathophysiology. Acta Pharmacol Sin 27:773–780 [PubMed: 16787559]

87. Verkhratsky A, Rodriguez JJ, Parpura V (2012) Calcium signalling in astroglia. Mol Cell Endocrinol 353:45–56 [PubMed: 21945602]

88. Guerra-Gomes S, Sousa N, Pinto L, Oliveira JF (2017) Functional Roles of Astrocyte Calcium Elevations: From Synapses to Behavior. Front Cell Neurosci 11:427 [PubMed: 29386997]

89. Torres-Ceja B, Olsen ML (2022) A closer look at astrocyte morphology: Development, heterogeneity, and plasticity at astrocyte leaflets. Curr Opin Neurobiol 74:102550 [PubMed: 35544965]

90. Aboufares El Alaoui A, Jackson M, Fabri M, de Vivo L, Bellesi M (2020) Characterization of Subcellular Organelles in Cortical Perisynaptic Astrocytes. Front Cell Neurosci 14:573944 [PubMed: 33633542]

91. Gavrilov N, Golyagina I, Brazhe A, Scimemi A, Turlapov V, Semyanov A (2018) Astrocytic Coverage of Dendritic Spines, Dendritic Shafts, and Axonal Boutons in Hippocampal Neuropil. Front Cell Neurosci 12:248 [PubMed: 30174590]

92. Patrushev I, Gavrilov N, Turlapov V, Semyanov A (2013) Subcellular location of astrocytic calcium stores favors extrasynaptic neuron-astrocyte communication. Cell calcium 54:343–349 [PubMed: 24035346]

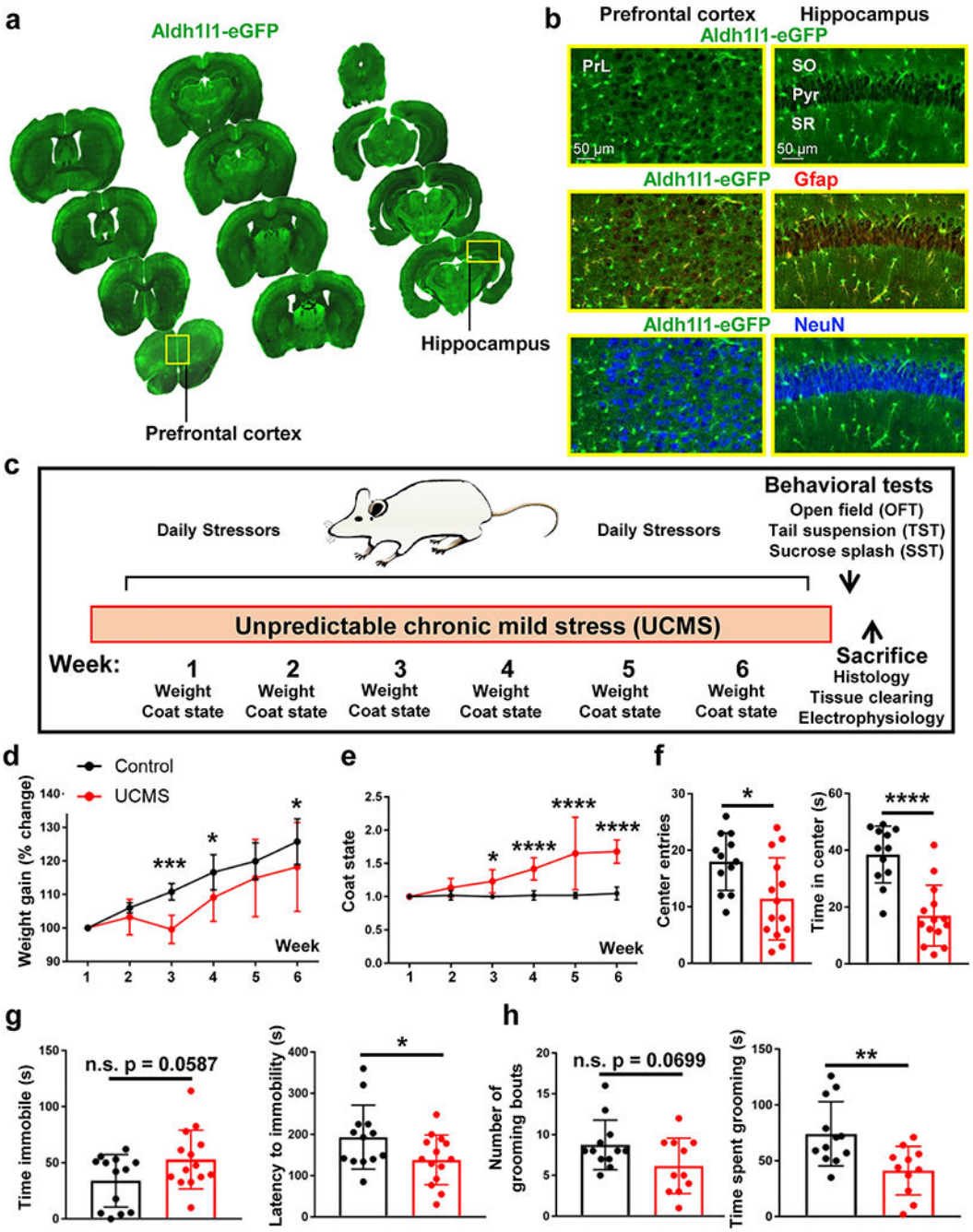

Figure 1: *Aldh1l1*-eGFP mouse and Unpredictable Chronic Mild Stress paradigm

(a) Coronal mouse brain sections from one *Aldh1l1*-eGFP. 30 μm thick tissue sections were mounted on slides at ~500 μm intervals to demonstrate transgene expression throughout the rostral-caudal and dorsal-ventral axis of the brain. Abbreviations: PrL = prelimbic cortex. (b) 20X representative images of the *Aldh1l1*-eGFP transgene in both the prefrontal cortex (left panel) and hippocampus (right panel). Note that *Aldh1l1*-eGFP positive cells co-localize with the astrocytic marker GFAP, but not with the neuronal marker NeuN. Abbreviations: SO = stratum radiatum; Pyr = pyramidal cell layer; SR = stratum radiatum (c) Schematic

outline of the six-week Unpredictable Chronic Mild Stress (UCMS) paradigm. (d) Percent change in weight over the six-week UCMS paradigm in control (black line) and UCMS (red line) mice. Data were analyzed using ANOVA, followed by post-hoc tests. (e) Graphical representation of coat/fur state across the six-week UCMS paradigm. Data were analyzed using ANOVA, followed by post-hoc tests. (f) Graphical representation of number of center entries (left panel) and total time spent in the center or the arena (right panel) in the open field test. Data were analyzed using Student's t-test. g) Graphical representation of the amount of time spent immobile (left panel) and the latency to the first immobility (right panel) in the tail suspension test. Data were analyzed using Student's t-test. (h) Graphical representation of the number of total grooming bouts (left panel) and the amount of time spent grooming (right panel) in the sucrose splash test. Data were analyzed using Student's t-test. *: $p < 0.05$; **: $p < 0.01$; ***: $p < 0.001$; ****: $p < 0.0001$; n.s.: not significant. N = 11-14 animals per condition.

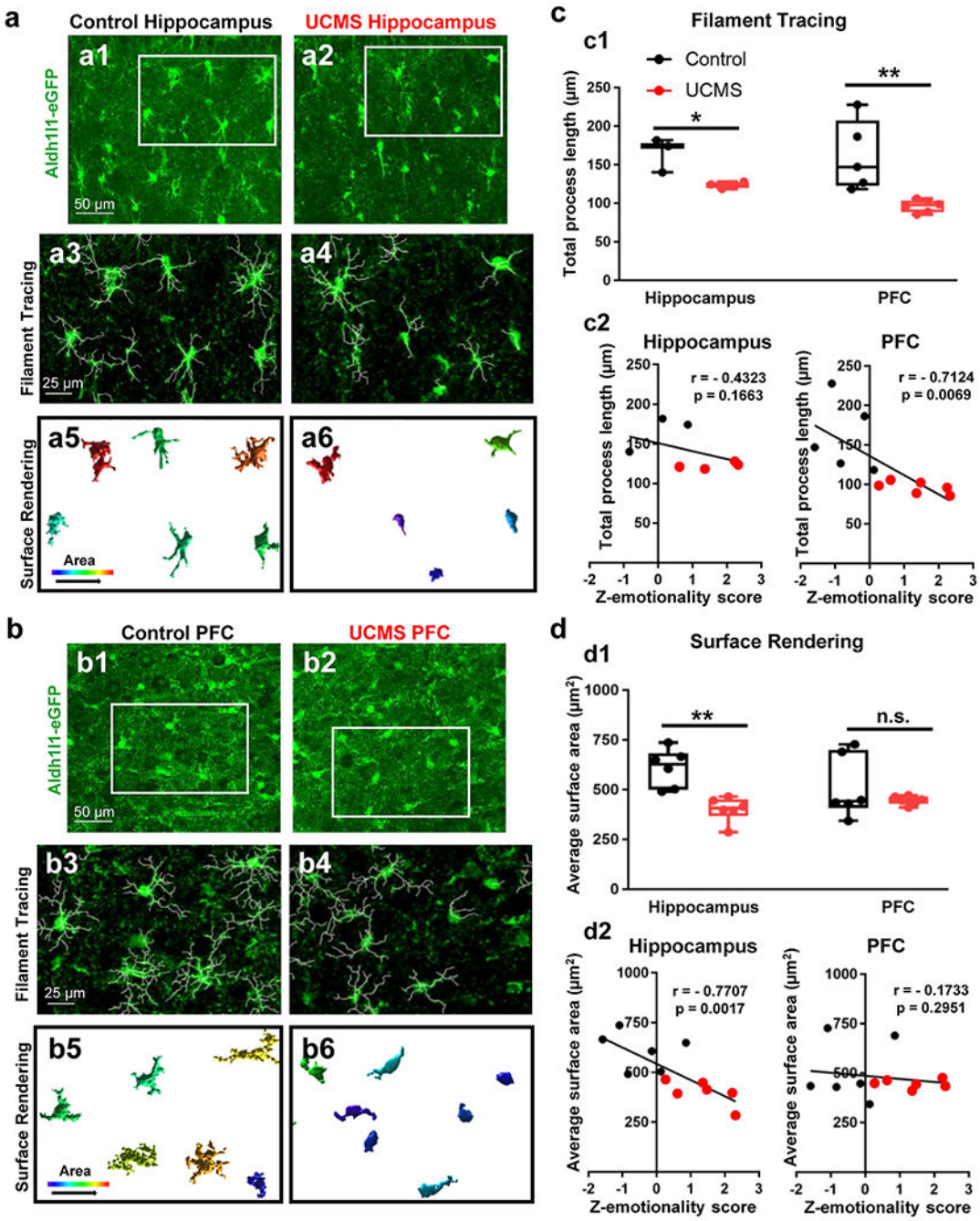

Figure 2: Changes in astrocyte morphology after UCMS

(a1-a2) Representative 40X confocal images of *Aldh1l1*-GFP transgene in the hippocampus of a control (left panel) and stressed animal (right panel). The regions boxed in white reflect the same areas depicted in 'a3-a4'. (a3-a4) Imaris filament tracing of astrocyte processes from a control (left panel) and UCMS (right panel) animal. (a5-a6) Imaris 3D-surface rendering of the same astrocytes depicted in 'a1-a4'. Note the relative increase in area of astrocytes in the control section relative to the UCMS section. (b1-b2) Representative 40X confocal images of *Aldh1l1*-GFP transgene in the PFC of a control (left panel) and stressed

animal (right panel). The regions boxed in white reflect the same areas depicted in ‘b3-b4’. (b3-b4) Imaris filament tracing of astrocyte processes from the PFC of a control (left panel) and UCMS (right panel) animal. (b5-b6) Imaris 3D-surface rendering of the same astrocytes depicted in ‘b1-b4’. (c1) Graphical analysis of Imaris filament tracing in hippocampal and PFC astrocytes from control animals (black) and UCMS animals (red). The average total astrocyte process length for each animal (analyzed from 3-4 images) is represented by each dot. Data were analyzed using Student’s t-test. *: $p < 0.05$; **: $p < 0.01$. N = 3-6 animals per stress condition. (c2) Graphical representation of correlations between average astrocyte process length (from hippocampal astrocytes: left panel and PFC astrocytes: right panel) and Z-emotionality behavioral scores. Correlations were analyzed using mice from both control (black dots) and UCMS (red dots) mice. A one-tailed Pearson analysis (using the ‘R correlation coefficient’) was used. N = 3-6 animals per condition. (d1) Graphical analysis of average astrocyte area (using Imaris 3D surface rendering) in hippocampal and PFC astrocytes from control animals (black) and UCMS animals (red). The average total astrocyte process area for each animal (analyzed from 3-4 images) is represented by each dot. Data were analyzed using Student’s t-test. **: $p < 0.01$; n.s.: not significant. N = 6 animals per stress condition. (d2) Graphical representation of correlations between average astrocyte process area (from hippocampal astrocytes: left panel and PFC astrocytes: right panel) and Z-emotionality behavioral scores. Correlations were analyzed using mice from both control (black dots) and UCMS (red dots) mice. A one-tailed Pearson analysis (using the ‘R correlation coefficient’) was used. N = 6 animals per condition.

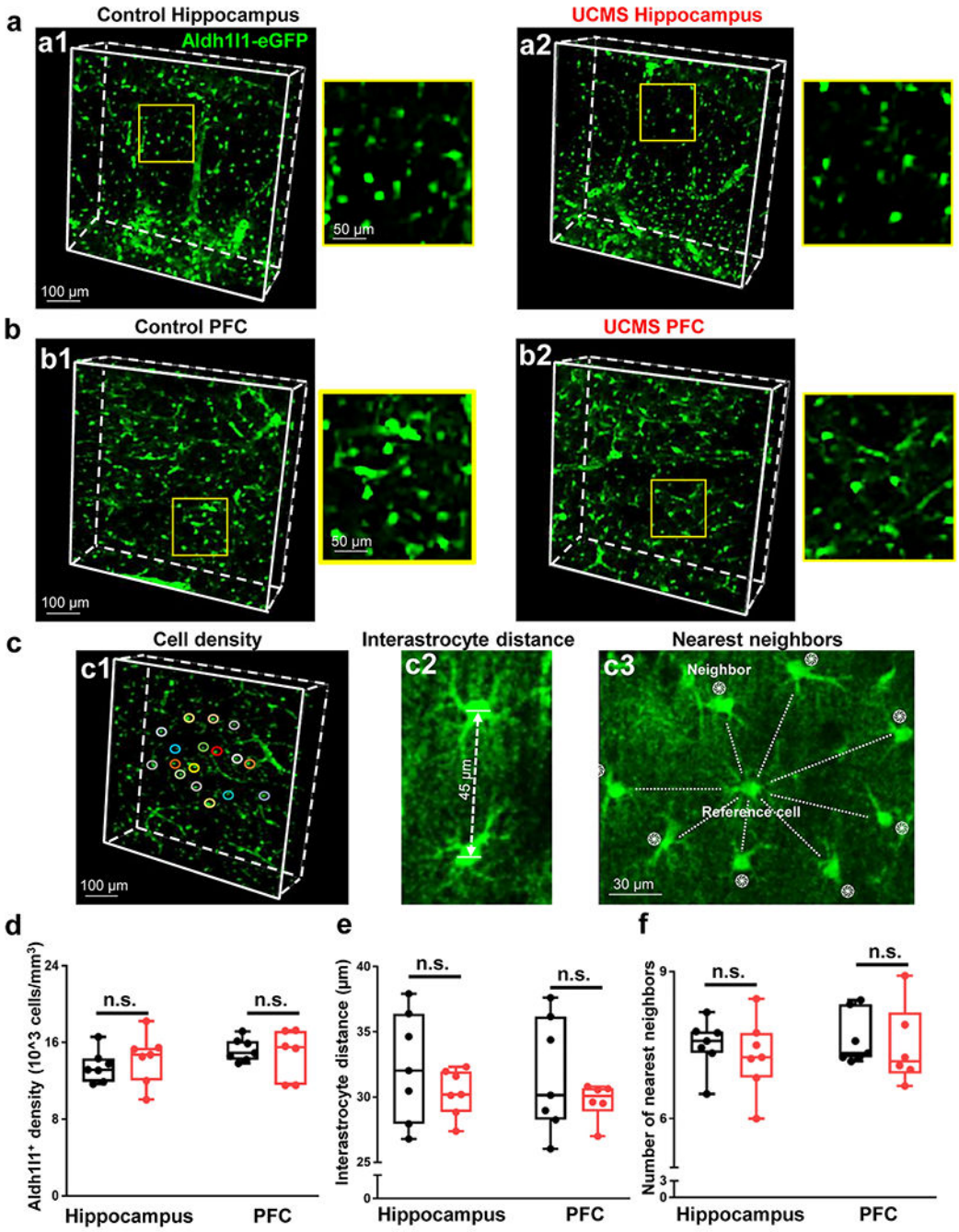

Figure 3: CUBIC tissue clearing in hippocampus and PFC of *Aldh1l1*-eGFP animals

(a1-a2) Representative 10X CUBIC tissue clearing in the hippocampus of a control (left panel) and UCMS (right panel) animal. Note that the yellow box in the larger panels approximate the locations of the zoomed-in images on the right. (b1-b2) Representative 10X CUBIC tissue clearing in the PFC of a control (left panel) and UCMS (right panel) animal. (c1) Representation of astrocyte syncytial cell density analysis, interastrocyte distance (c2), and nearest neighbors (c3). (d) Graphical representation of the density of *Aldh1l1*-eGFP positive cells in the hippocampus (left) and PFC (right) of control and

stressed animals. Data was analyzed from 6-7 animals per condition using Student's t-test. (e) Graphical representation of the interastrocyte distance (i.e., the distance between astrocytes) in the hippocampus (left) and PFC (right) of control and stressed animals. (f) Graphical representation of the number of neighboring astrocytes nearest to the reference cell/astrocyte. Data was analyzed from 6-7 animals per condition using Student's t-test. n.s.: not significant.

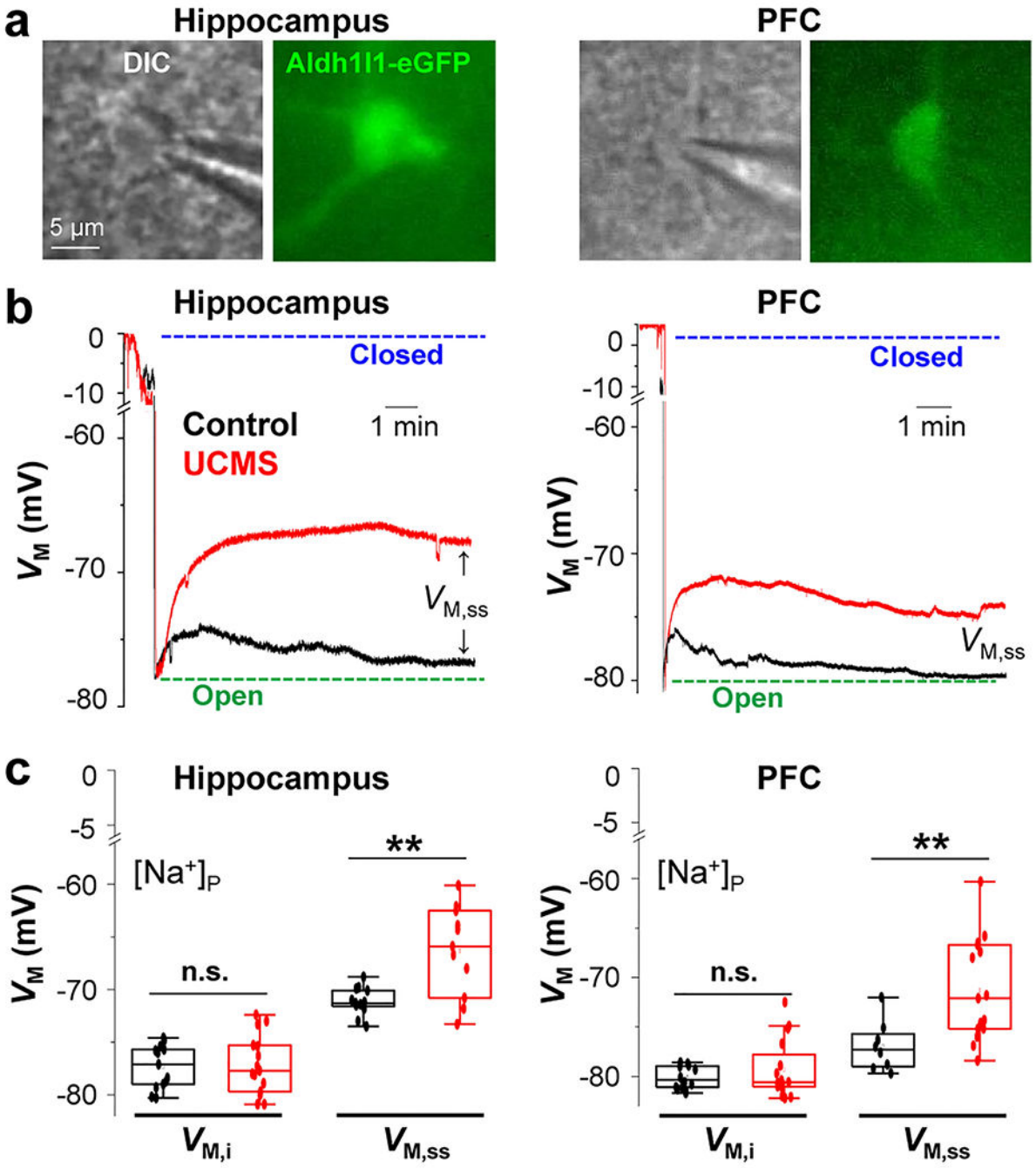

Figure 4: UCMS impairs the strength of astrocyte syncytial coupling within the hippocampus and PFC

(a) Astrocytes recorded from hippocampal (left) and PFC (right) brain slices (DIC images and *Aldh1l1*-eGFP fluorescent images for astrocyte identification). (c and d) Representative electrophysiological traces from astrocytes recorded with K^+ free-Na^+ containing electrode $[Na^+]_P$ in the hippocampus (c) and PFC (e) from control (black trace) and UMCS (red trace) animals. The initial V_M ($V_{M,i}$) was determined immediately after the breakthrough of the cell membrane in whole-cell recording. The steady-state V_M ($V_{M,ss}$) was determined 10-15 min after the membrane breakthrough and was used as a readout of gap junctional

coupling strength between astrocytes. Astrocytes recorded from UCMS slices of both the hippocampus and PFC displayed a positive shift of $V_{M,\,ss}$ which corresponds to a weakened syncytial coupling strength. (d and f) Graphical representation of $V_{M,\,i}$ and $V_{M,\,ss}$ in hippocampus and PFC astrocytes from control (black) and UCMS-exposed (red) animals. For both hippocampal and PFC regions, 6-16 astrocytes were recorded. Data is presented as the mean ± SEM using Student's t-test. **: $p < 0.01$; n.s.: not significant.

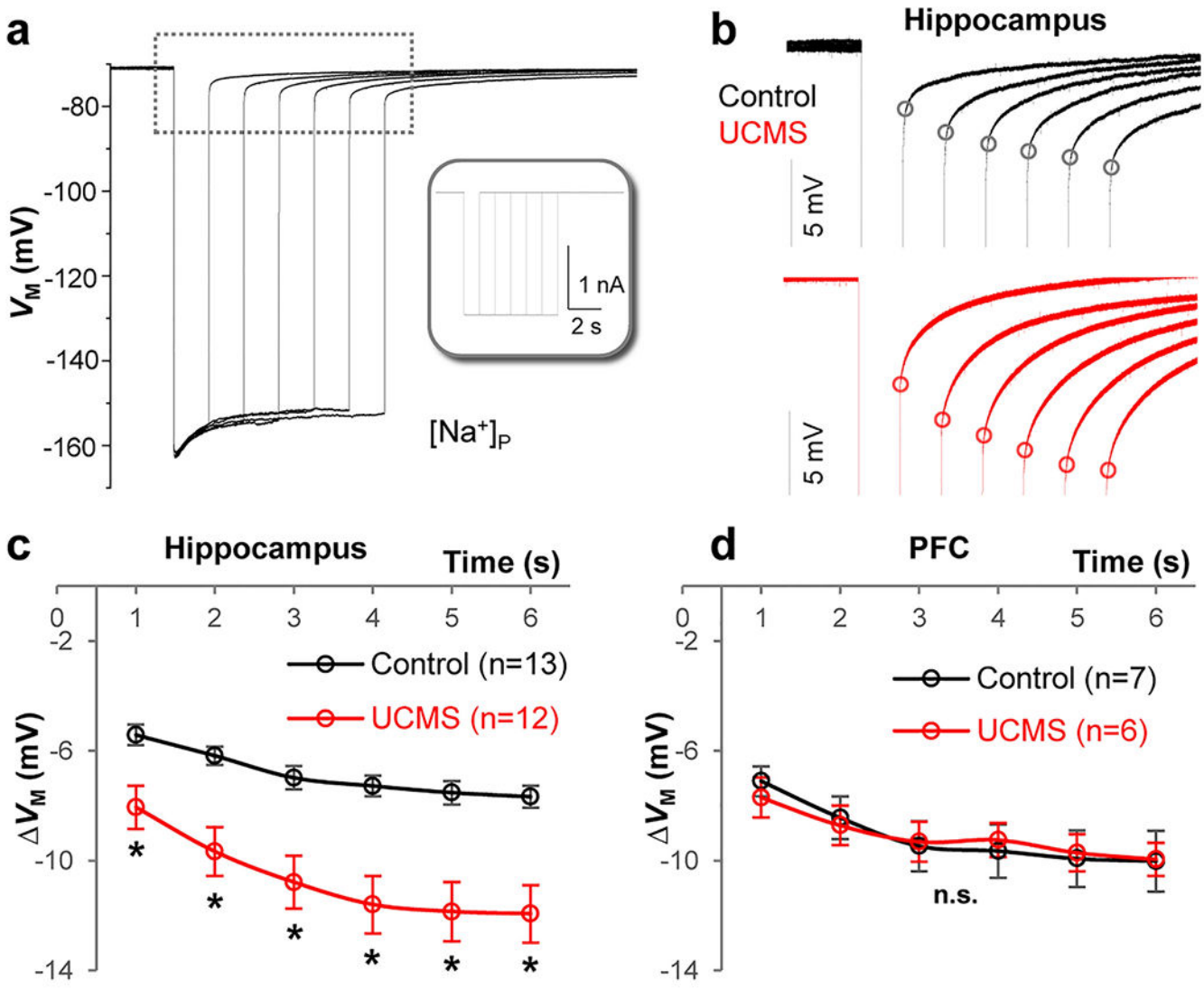

Figure 5: UCMS impairs the K^+ redistribution capacity of an astrocyte syncytium

(a) Representative trace recorded with K^+ free-Na^+ containing electrode $[Na^+]_P$ in current-clamp mode. Inset: −2 nA current steps ($I_{holding}$) were applied at incremental durations from 1 to 6 s. In between these steps, the cell was maintained at resting condition for V_M recovery. The longer the duration of the current steps, the stronger the negative shift in the reversal potential (V_{rev}, black dots) upon withdrawal of the steps, indicating more accumulation of K^+ inside astrocytes. (b) Enlarged recording trace (indicated by dashed line area in a) of astrocytes in the hippocampus from control (black) and UCMS (red) animals. The ΔV_M is the difference between the basal V_M and V_{rev} values and is used to compare the capacity of K^+ redistribution in different groups. (c) In the hippocampus, the increased ΔV_M in the UCMS group indicates weakened capacity of K^+ redistribution of the astrocyte syncytium. (d) In the PFC, there was no significant difference of ΔV_M between control and UCMS groups. Two-Way Mixed-Design ANOVA. *: $p < 0.05$. n.s.: not significant. n = 6-13 recorded cells per group.

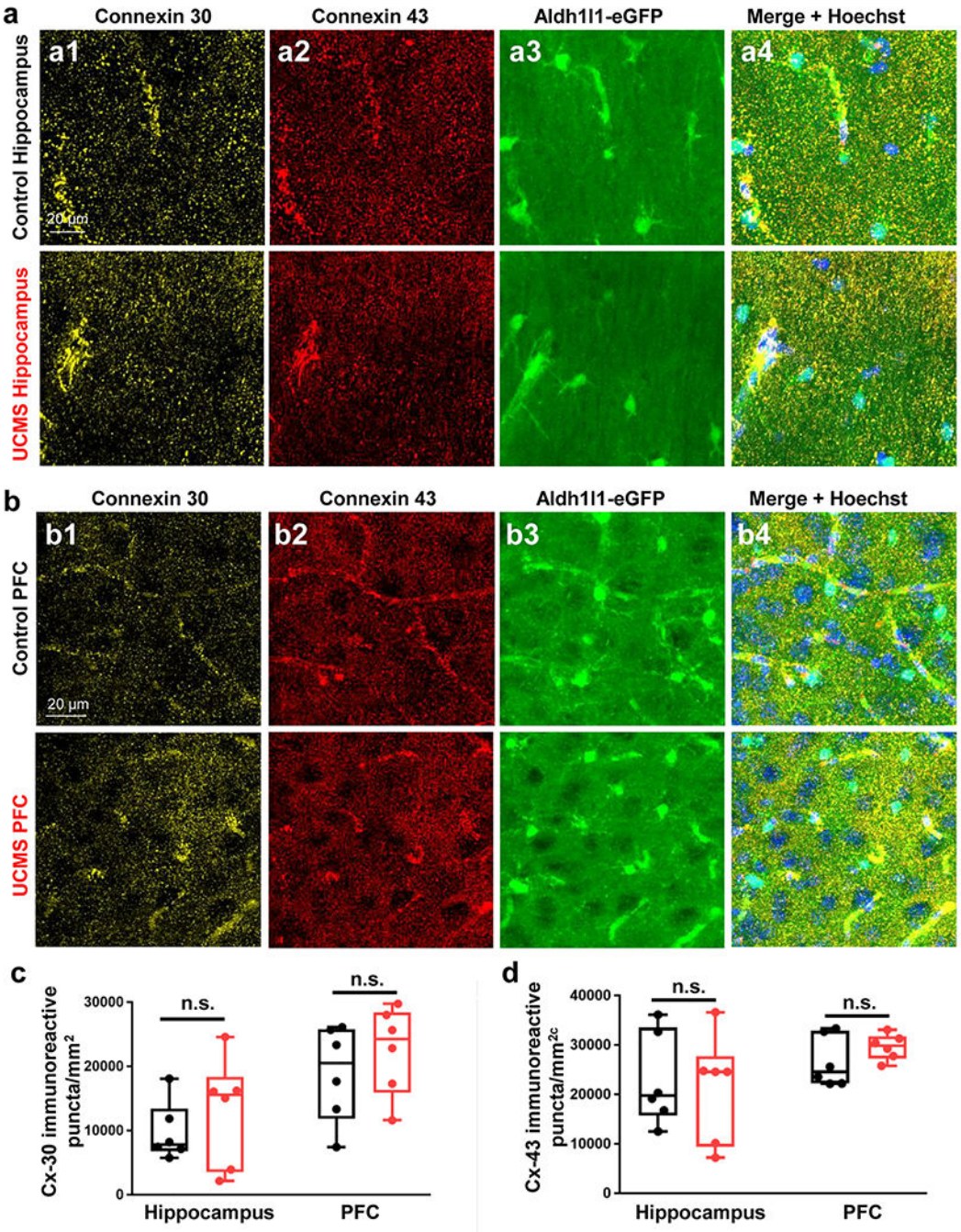

Figure 6: UCMS does not alter the number of connexin 30 (Cx30) or connexin 43 (Cx43)-immunoreactive puncta in the hippocampus or PFC

(a1-a4) Representative 40X immunofluorescent images of connexin 30 (yellow), connexin 43 (red), *Aldh1l1*-eGFP transgene (green), and Hoechst (blue) in the stratum radiatum of the hippocampus of control (top row) and UCMS exposed (bottom row) animals. (b1-b4) Representative 40X immunofluorescent images of connexin 30 (yellow), connexin 43 (red), *Aldh1l1*-eGFP transgene (green), and Hoechst (blue) in the PFC of control (top row) and UCMS exposed (bottom row) animals. (c) Graphical representation of the number of connexin 30 immunoreactive puncta per area of hippocampus/PFC in control and UCMS

mice. (d) Graphical representation of the number of connexin 43 immunoreactive puncta per area of hippocampus/PFC in control and UCMS mice. Data were analyzed using Student's t-test. n.s.: not significant. N = 6 animals per condition.

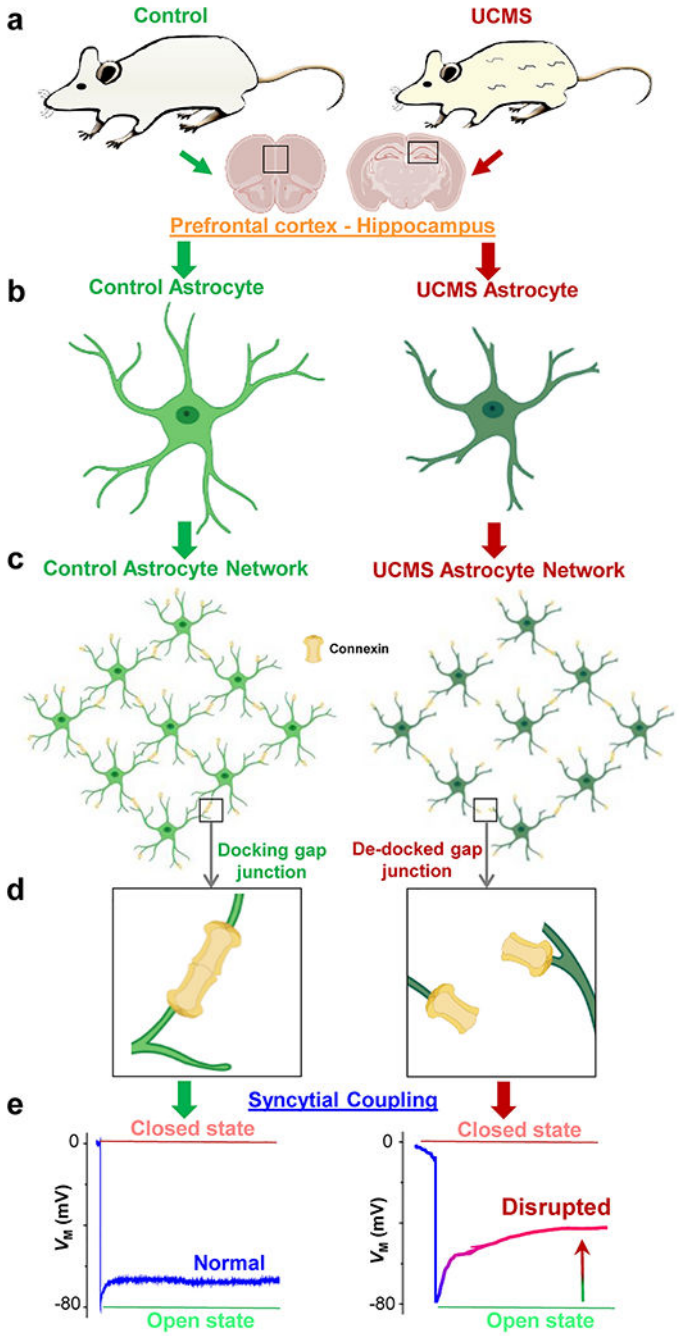

Figure 7: Schematic overview and hypothesized model of gap junction coupling after UCMS

(a) Representative cartoon images of a control (left panel) and UCMS (right panel) mouse. Note the discoloration and tufts in the fur of the UCMS animal after the six-week stress paradigm. Information depicted in the schematic (and in the paper) was obtained from astrocytes within two brain regions: the prefrontal cortex (PFC) and the hippocampus. (b-c) Representation of control (light green) and UCMS (dark green) astrocyte morphology (both individual and network-level). Note the shrinkage of astrocytic processes from UCMS mice. Connexins are represented in yellow. (d) Hypothesized mechanism of gap junction coupling:

unlike connexins in astrocytic processes from control animals (left panel) which successfully dock, connexins from astrocyte processes of UCMS animals may not be able to properly 'dock' (i.e., many connexins 'de-dock'), leading to weakened coupling. (e) Representation of the electrophysiological readout (based on our recorded results) of syncytial coupling strength in astrocytes from the PFC and hippocampus of control (left panel) and UCMS (right panel) animals. Note the decreased coupling strength in astrocytes from UCMS mice. PFC and hippocampus brain sections, astrocytes, and connexins were created with BioRender software.

Table 1:

Example six-week UCMS schedule

Sunday	Monday	Tuesday	Wednesday	Thursday	Friday	Saturday
Tail cramp (1 min) Heat stimulation (10 min)	Restraint (2 hrs) Loud music (3 hrs) Exposure to empty water bottle (overnight)	Wet bedding (3 hrs) 45° cage tilt (7 hrs)	Shake on rocker (1 hr) Cold exposure (30 mn) Spray with water (5 min)	No bedding (4 hrs) Heat stimulation (10 min) Restraint (2 hrs)	Loud music (3 hrs) Crowded space (1 hr)	Spray with water (5 min) Tail cramp (1 min) 45° cage tilt (overnight)

Mice were exposed to 2-3 stressors each day for a period of six consecutive weeks. Of note, to prevent animals from habituating to the daily stressors, these stressors were performed at different times throughout the day (i.e., in the morning, afternoon, evening, and overnight).